

This is the accepted manuscript made available via CHORUS. The article has been published as:

Large magnetic thermal conductivity induced by frustration in low-dimensional quantum magnets

Jan Stolpp, Shang-Shun Zhang, Fabian Heidrich-Meisner, and Cristian D. Batista

Phys. Rev. B **99**, 134413 — Published 9 April 2019

DOI: [10.1103/PhysRevB.99.134413](https://doi.org/10.1103/PhysRevB.99.134413)

Large magnetic thermal conductivity induced by frustration in low-dimensional quantum magnets

Jan Stolpp,^{1,2} Shang-Shun Zhang,³ Fabian Heidrich-Meisner,¹ and Cristian D. Batista^{3,4}

¹*Institut für Theoretische Physik, Georg-August-Universität Göttingen, D-37077 Göttingen, Germany*

²*Physics Department and Arnold Sommerfeld Center for Theoretical Physics,
Ludwig-Maximilians-Universität München, D-80333 München, Germany*

³*Department of Physics and Astronomy, University of Tennessee, Knoxville, Tennessee 37996-1200, USA*

⁴*Quantum Condensed Matter Division and Shull-Wollan Center,
Oak Ridge National Laboratory, Oak Ridge, Tennessee 37831, USA*

We study the magnetic field-dependence of the thermal conductivity due to magnetic excitations in frustrated spin-1/2 Heisenberg chains. Near the saturation field, the system is described by a dilute gas of weakly-interacting fermions (free-fermion fixed point). We show that in this regime the thermal conductivity exhibits a non-monotonic behavior as a function of the ratio $\alpha = J_2/J_1$ between second and first nearest-neighbor antiferromagnetic exchange interactions. This result is a direct consequence of the splitting of the single-particle dispersion minimum into two minima that takes place at the Lifshitz point $\alpha = 1/4$. Upon increasing α from zero, the inverse mass vanishes at $\alpha = 1/4$ and it increases monotonically from zero for $\alpha \geq 1/4$. By deriving an effective low-energy theory of the dilute gas of fermions, we demonstrate that the Drude weight K_{th} of the thermal conductivity exhibits a similar dependence on α near the saturation field. Moreover, this theory predicts a transition between a two-component Tomonaga-Luttinger liquid and a vector-chiral phase at a critical value $\alpha = \alpha_c$ that agrees very well with previous density matrix renormalization group results. We also show that the resulting curve $K_{\text{th}}(\alpha)$ is in excellent agreement with exact diagonalization (ED) results. Our ED results also show that $K_{\text{th}}(\alpha)$ has a pronounced minimum at $\alpha \approx 0.7$ and it decreases for sufficiently large α at lower magnetic field values. We also demonstrate that the thermal conductivity is significantly affected by the presence of magnetothermal coupling.

I. INTRODUCTION

Frustration leads to many fascinating phenomena in quantum magnets, such as the partial or complete suppression of magnetic order or the stabilization of spin-liquid phases with fractional excitations^{1–3}. These phenomena are particularly prevalent in reduced spatial dimensions, where quantum fluctuations become increasingly stronger. An even richer interplay of quantum fluctuations, frustration and interactions emerges in the presence of external magnetic fields. Several quantum phases with quite unusual properties were predicted, including spin-nematic behavior or multipolar order^{4–15} and vector-chiral phases^{16–22}.

From the experimental point of view, an open question concerns predictions for clear fingerprints of such states with unconventional magnetic order in actual measurements (see e.g., Refs. 15, 23–25 for work in this direction). Moreover, many of the theoretical predictions apply to the ground-state phases of one-dimensional systems such as frustrated spin-1/2 chains^{10,11,17–20,26–28}, calling for investigations of the influence of temperature and a weak inter-chain coupling that is unavoidably present in real materials. Such questions were indeed addressed in, e.g., Refs. 27, 29–32 and Refs. 33–35, respectively.

Our work will be concerned with the vector-chiral phase at finite magnetizations, which is characterized by a finite expectation value of the vector chirality

$$\kappa_{ij}^{\text{vc}} = \langle (\vec{S}_i \times \vec{S}_j) \cdot \hat{z} \rangle. \quad (1)$$

Here, \hat{z} is the unit vector along the z -direction, which is the direction of the applied magnetic field and \vec{S}_i is the spin-S operator for site i . The vector-chiral phase breaks a discrete Z_2

symmetry and can thus be stabilized even in one-dimensional systems. In fact, several theoretical papers have established its existence in frustrated spin-1/2 chain Hamiltonians with a dominant Heisenberg exchange^{16–20,36}

$$\mathcal{H} = J \sum_{i=1}^N [\vec{S}_i \cdot \vec{S}_{i+1} + \alpha \vec{S}_i \cdot \vec{S}_{i+2} - B S_i^z], \quad (2)$$

where J and αJ are the nearest and next-to-nearest neighbor exchange couplings and B denotes the magnetic field (we set the Bohr magneton μ_B and the gyromagnetic factor g and \hbar to unity, N is the number of sites and we impose periodic boundary conditions). Several materials provide close realizations of this and related models, in particular, materials with a nearest-neighbor ferromagnetic exchange $J < 0$ and $\alpha < 1$, such as LiCuVO_4 ^{37–41}, CuCl_2 ⁴², LiCu_2O_2 ^{43,44}, $\text{Li}_2\text{ZrCuO}_4$ ⁴⁵, LiCuSbO_4 ^{46,47}, $\text{PbCuSO}_4(\text{OH})_2$ ^{48–50} or $\text{Ca}_2\text{Y}_2\text{Cu}_5\text{O}_{10}$ ⁵¹, where often saturation fields are much lower than on the antiferromagnetic side ($J, \alpha > 0$). The synthesis of this list of materials, as well as the rich finite-magnetic field phase-diagram has motivated a large number of theoretical studies (see, e.g., Refs. 10, 11, 18, 20, 29, and 31). Earlier, materials with both $J > 0$ and $\alpha > 0$ were known such as SrCuO_2 ^{52–54} or CuGeO_3 ⁵⁵.

The main goal of our work is to establish a connection between frustration and *thermal conductivity* just below the saturation field. We will contrast the high-field behavior against the behavior at small magnetic fields. A very active research on thermal transport in low-dimensional quantum magnets^{56–68} was stimulated by a series of experiments^{69–77} revealing a significant magnetic contribution to the thermal conductivity (see Refs. 78 and 79 for a review). Much theoretical work was devoted to the transport properties of in-

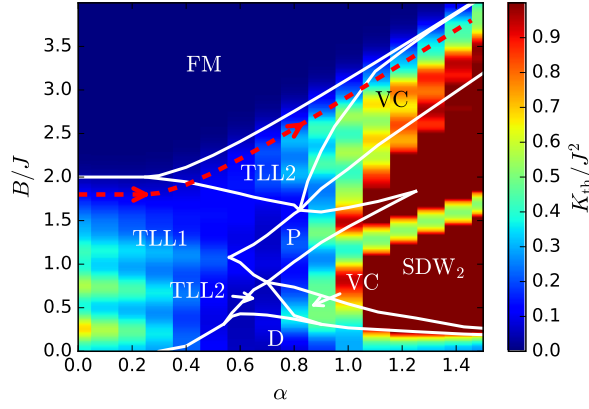


FIG. 1. (Color online) (B, α) quantum phase diagram of the frustrated spin-1/2 chain described by Eq. (2) with $\alpha > 0$. Solid, white lines are the $(T = 0)$ phase boundaries taken from Ref. 19. The ground-state phases are: one- and two-component Tomonaga-Luttinger liquid phases (TLL1 and TLL2), a dimer phase (D), a 1/3-plateau phase (P), a spin-density wave phase where the lowest-lying excitations are two-magnon bound states (SDW_2), vector-chiral phases (VC) and the ferromagnetic phase where all spins are aligned with the external field B (FM). The coloring shows the strength of the thermal Drude weight K_{th} as defined in Eq. (15), computed with exact diagonalization with $N = 16$ sites for a low temperature $T/J = 0.1$. To improve the results of the exact diagonalization we also performed an average over different twisted boundary conditions with 10 different values of the twist angle as explained in Sec. V A. The dashed line indicates the magnetic field region just below saturation that is our work's main interest: we follow the evolution of the thermal conductivity as α increases.

tegrable spin chains, which can exhibit ballistic transport⁸⁰. The best-known example is the spin-1/2 XXZ chain, which is a perfect thermal conductor at any finite temperature and for any strength of the exchange anisotropy^{64,65,80}. This peculiar behavior manifests itself in a small or even vanishing finite-frequency contribution $\kappa_{\text{reg}}(\omega)$, but a finite thermal Drude weight K_{th} . Formally, this corresponds to decomposing the thermal conductivity κ into

$$\text{Re } \kappa(\omega) = K_{\text{th}}\delta(\omega) + \kappa_{\text{reg}}(\omega). \quad (3)$$

Even in the absence of external scattering mechanisms, nonintegrable spin systems are believed to be normal diffusive thermal conductors with a vanishing Drude weight in the thermodynamic limit^{58,62,81–83}. This notably includes frustrated spin-1/2 chains^{58,84}. For finite-size systems, the thermal Drude weight is still large in comparison to the total weight of $\text{Re } \kappa(\omega)$, in particular at low temperatures. In certain parameter regions, other aspects factor in. For instance, the proximity to the integrable $\alpha = 0$ model plays a role and a particularly weak breaking of the energy-current conservation is realized in frustrated chains for small α ⁸⁴ (as compared to other nonintegrable models^{62,83}). In addition, the effective low-energy theory becomes a free-fermion fixed point at the saturation field, implying that a similar situation should be expected in this regime.

We employ two approaches to study the thermal conduc-

tivity: first, a dilute-gas treatment near saturation, which correctly predicts the existence of the vector-chiral phase and the transition point α_c . This approach is complemented with exact diagonalization to provide independent support for the predictions in the dilute-gas regime. Exact diagonalization provides full access to $\kappa(\omega)$ but is limited to system sizes of $N \sim 20$ sites if the full spectrum is needed. As a consequence, the low-frequency and low-temperature regime can suffer from strong finite-size effects. Inspired by Ref. 85, we demonstrate that in the high-field regime, these finite-size effects can be reduced by using twisted boundary conditions and averaging over different twist angles. Using this flux-averaging could be, in general, a strategy to mitigate finite-size effects in exact-diagonalization studies of frustrated spin systems.

Since we will be interested in the evolution of the thermal conductivity as a function of α at both low and high fields, the proximity to exactly solvable points (or regimes with very long-lived excitations) will result in $K_{\text{th}} \sim O(I_{\text{th}}^0)$ on small, finite systems, where I_{th}^0 is the total weight in $\text{Re } \kappa(\omega)$. Thus, while we expect that $K_{\text{th}}(\alpha \neq 0) \rightarrow 0$ for very large systems^{58,81}, we will focus on Drude weights as a measure of the low-frequency behavior due to the particular parameter regimes of interest and the limitations of exact diagonalization. In the simplest picture, we can think of the zero-frequency delta function in Eq. (3) acquiring a finite width as α becomes nonzero (assuming the thermodynamic limit now), with the Drude weight being a measure of the integral over this low-frequency peak.

Given that we will mostly deal with thermal transport in finite magnetic fields, the spin analogue of the electronic Seebeck effect must be taken into account due to the coupling between the energy current and the spin current as $B > 0$. This yields a correction to the thermal conductivity just as for electrons, which is often dubbed magnetothermal correction^{66,67,86–88}. Whether or not such magnetothermal corrections exist in real materials is an open question, with some experiments suggesting their absence⁸⁹, presumably due to spin-orbit coupling. Regardless of these considerations, we will consider the transport coefficients both including and ignoring such magnetothermal corrections and will elucidate the similarities and differences.

We will consider the case of competition between nearest and next-nearest-neighbor antiferromagnetic exchange interactions, $J > 0$ and $\alpha > 0$, in the presence of an external magnetic field B . The quantum phase diagram of this model is well known by now^{19,90,91}. Figure 1 shows the field versus α phase diagram adapted from Ref. 19. The zero-field ground state is a Tomonaga-Luttinger (TLL) liquid for $\alpha < \alpha_d$ and a dimerized state for $\alpha > \alpha_d \approx 0.241\dots$ ^{92–94}. This implies that $K_{\text{th}} \propto vT$ (v is the Fermi velocity) for $\alpha < \alpha_d$, while $K_{\text{th}} \propto e^{-\Delta(\alpha)/k_B T}$ for $\alpha > \alpha_d$, at low enough temperature, where $\Delta(\alpha)$ is the gap of the dimerized phase. In other words, K_{th} is strongly suppressed as a function of increasing α (or frustration) at zero magnetic field. We note, however, that the spin gap $\Delta(\alpha)$ is a non-monotonic function of α ⁹³, implying that $K_{\text{th}}(T, B, \alpha)$ must reach its minimum value at the finite α value that maximizes the $B = 0$ spin gap.

In the opposite end of the phase diagram, when the mag-

netic field reaches its saturation value $B = B_{\text{sat}}$, the critical boundary $B = B_{\text{sat}}(\alpha)$ is described by a free-fermion fixed point. Thermodynamic properties are then very well described with a slightly renormalized version of the bare single-particle dispersion,

$$\epsilon_k(\alpha) = J(\cos k + \alpha \cos 2k - \cos Q - \alpha \cos 2Q), \quad (4)$$

which is obtained by rewriting \mathcal{H} in terms of spinless-fermion operators via a Jordan-Wigner transformation⁹⁵. As expected, the behavior of K_{th} near $B = B_{\text{sat}}$ is also basically determined by the dispersion relation $\epsilon_k(\alpha)$. The condition $B \simeq B_{\text{sat}}$ sets the Fermi level of the spinless fermions near the bottom of the band $\epsilon_k(\alpha)$, i.e., in the region where $\epsilon_k(\alpha)$ can be approximated by a parabolic dispersion with an effective mass $m^*(\alpha)$. Consequently, K_{th} has a universal temperature dependence parametrized by the single parameter $m^*(\alpha)$ at low enough temperature.

The effective mass $m^*(\alpha)$ is obtained by expanding $\epsilon_k(\alpha)$ around its minimum value. $\epsilon_k(\alpha)$ has a single minimum at $Q = \pi$ for $\alpha \leq 1/4$ and two minima at $\pm Q$ with $\cos Q = -1/(4\alpha)$ for $\alpha > 1/4$ (we set the lattice spacing to unity). It is clear from Eq. (4) that $\epsilon_Q(\alpha) = 0$ and that the dispersion is quadratic around $k = Q$ (the dynamical exponent is $z = 2$). The inverse of the effective mass $[m^*(\alpha)]^{-1} = \partial^2 \epsilon_k / \partial^2 k|_{k=Q}$ is:

$$\begin{aligned} \frac{1}{m^*(\alpha)} &= J(1 - 4\alpha) \quad \text{for } \alpha < 1/4 \\ \frac{1}{m^*(\alpha)} &= J \left[4\alpha - \frac{1}{4\alpha} \right] \quad \text{for } \alpha > 1/4. \end{aligned} \quad (5)$$

As shown in Fig. 2, $1/m^*(\alpha)$ is a non-monotonic function of α : it decreases (increases) with α for $\alpha < 1/4$ ($\alpha > 1/4$). The point $\alpha = 1/4$ corresponds to the Lifshitz transition point with a divergent effective mass ($m^* \rightarrow \infty$ because the dispersion relation becomes quadratic around $k = \pi$). The thermal conductivity is $K_{\text{th}} \propto T^{3/2} / \sqrt{m^*}$ for a free-fermion fixed point. Consequently, the non-monotonic behavior of $1/m^*(\alpha)$ implies a non-monotonic behavior of $K_{\text{th}}(\alpha)$ near the saturation field. Moreover, given that $K_{\text{th}} \propto \sqrt{J\alpha} T^{3/2}$ for $\alpha \gg 1/4$, K_{th} increases with α for $\alpha > 1/4$, in contrast to the zero-field case.

The increase of K_{th} with α becomes even more pronounced for the Tomonaga-Luttinger liquid phase that exists right below the saturation field B_{sat} . The simple reason is that $K_{\text{th}} \propto vT$ at low enough T , where v is the (renormalized) velocity of the excitations that now have a linear dispersion $E(q) = vq$ near the Fermi level ($q = k - k_f$, where k_f is the Fermi wave vector). As long as $B \lesssim B_{\text{sat}}$, the particle density ρ remains very low, implying that the interactions produce a very small renormalization of the Fermi velocity: $v \simeq \rho\pi/m^*$. In terms of the original magnetic moments, the particle density is given by $\rho = (M_{\text{sat}} - M)$, where $M = \sum_j \langle S_j^z \rangle / N$ is the magnetization per site, $M_{\text{sat}} = 1/2$ is its saturation value and N is the total number of sites. Consequently, $v \simeq (M_{\text{sat}} - M)/m^*$ and $K_{\text{th}} \propto vT \simeq \sqrt{B_{\text{sat}} - B} T / m^*$, implying that $K_{\text{th}} \propto \alpha T \sqrt{B_{\text{sat}} - B}$ for $\alpha \gg 1/4$. In other words, $K_{\text{th}}(\alpha)$ becomes much bigger than $K_{\text{th}}(0)$ (for a fixed value of M) for $\alpha \gg 1/4$. Given that the

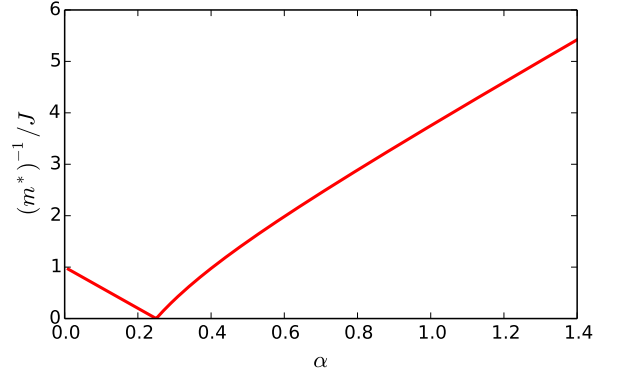


FIG. 2. (Color online) Evolution of the effective mass at the saturation field as a function of the frustration parameter α .

vector-chiral phase appears for $\alpha \gtrsim 1.3$ (see Fig. 1), the system must be in that phase for $K_{\text{th}}(\alpha)$ to be five times bigger than $K_{\text{th}}(0)$ (see Fig. 2). However, we emphasize that the increase of $K_{\text{th}}(\alpha)$ is not related to the emergence of the vector-chiral phase, but to the change in the single-particle spectrum.

Our analysis indicates that K_{th} should depend strongly on the applied magnetic field. For large enough values of α and a fixed value of $M \lesssim M_{\text{sat}}$, $K_{\text{th}}(\alpha)/K_{\text{th}}(0) \simeq 4\alpha$, while $K_{\text{th}}(\alpha)/K_{\text{th}}(0) \propto e^{-\Delta(\alpha)/k_B T}$ for $M = 0$. Here, we show that this is indeed the case by combining exact-diagonalization results with simple analytical arguments. As a first account of our numerical results, Fig. 1 shows the thermal Drude weight K_{th} computed for $N = 16$ sites at $T/J = 0.1$. The main focus will be on large fields just below saturation: K_{th} clearly increases once the vector-chiral phase is entered (follow the dashed line in Fig. 1). By contrast, at low fields, K_{th} decreases away from $\alpha = 0$ in the TLL1 phase and becomes very small in the vicinity of the dimer phase D. The predicted field dependence of the magnetic contribution to the thermal conductivity could be experimentally verified in materials with a sufficiently small saturation field. In fact, the thermal transport properties of frustrated chains (with the exception of the spin-Peierls material CuGeO_3 ^{96,97}) are largely unexplored.

To conclude the introduction, we wish to alert the reader that the previous arguments are based on an approximation to the low-energy spectrum of \mathcal{H} (e.g., free bosons with linear spectrum in the TTL regime), which ignores the combined effect of irrelevant interactions (in the renormalization group sense) and deviations from linear dispersion^{98–100} and thus has a purely ballistic thermal transport. For a linear dispersion, $K_{\text{th}} \propto C_V v^2$, where C_V is the specific heat. However, this ballistic response becomes diffusive upon including the above-mentioned corrections, as well as extrinsic mechanisms, such as scattering off impurities, crystal imperfections and crystal boundaries. These extrinsic mechanisms give the dominant contribution to the relaxation time at very low temperatures, $1/\tau = 1/\tau_{\text{int}} + 1/\tau_{\text{ext}}$ because the relaxation time due to interactions between modes becomes arbitrarily long for $T \rightarrow 0$.

Our conclusions are thus subject to the assumption that extrinsic scattering does not introduce additional significant dependencies on the magnetic field or the frustration param-

ter α through the relaxation time τ . This, however, may be an unjustified assumption for certain materials in which spin-phonon coupling plays a dominant role^{61,63,101–105}. Thus, developing an understanding of thermal transport in frustrated spin-1/2 chains under incorporation of a spin-phonon coupling is left for future theoretical and experimental research.

This work is organized as follows. In Sec. II, we summarize the linear-response expressions for (coupled) spin and thermal transport. Section III describes the details of our exact-diagonalization analysis. In Sec. IV, we present a dilute Fermi-gas treatment that describes the regime near and above the saturation field for $\alpha \gg 1/4$. In Sec. V, we present our exact-diagonalization results. Section VI will provide a summary and discussion.

II. TRANSPORT COEFFICIENTS FROM LINEAR RESPONSE THEORY

We here introduce the linear-response expressions for the thermal conductivity from the Kubo formula¹⁰⁶. The expectation values of the spin and thermal currents, $j_1 = j_S$ and $j_2 = j_{th}$, are given by¹⁰⁶

$$\langle j_\mu \rangle = \sum_\nu L_{\mu\nu} f_\nu, \quad (6)$$

where $f_1 = \nabla B$ and $f_2 = -\nabla T$ refer to the magnetic field and temperature gradients. $L_{\mu\nu}$ is the conductivity matrix. j_1 and j_2 can be expressed via the spin and energy currents j_S and j_E by

$$j_1 = j_S, \quad j_2 = j_{th} = j_E - B j_S, \quad (7)$$

where

$$j_{S[E]} = i \sum_{l=1}^N [h_{l-2} + h_{l-1}, d_l + d_{l+1}] \quad (8)$$

with

$$h_l = J \vec{S}_l \cdot \vec{S}_{l+1} + \alpha J \vec{S}_l \cdot \vec{S}_{l+2} \quad (9)$$

and $d_l = h_l$ for the energy current and $d_l = S_l^z$ for the spin current.

The general expression for the coefficients $L_{\mu\nu}$ are ($\mu, \nu = th, S$)¹⁰⁶:

$$L_{\mu\nu}(\omega) = \frac{\beta^r}{N} \int_0^\infty dt e^{i(\omega + i0^+)t} \int_0^\beta d\tau \langle j_\mu j_\nu(t + i\tau) \rangle, \quad (10)$$

where $r = 0$ for $\nu = S$ and $r = 1$ for $\nu = th$.

As usual, the real part of the coefficients $L_{\mu\nu}$ is decomposed into a singular contribution at zero frequency and the regular part $L_{\mu\nu}^{\text{reg}}(\omega)$, with Drude weights $D_{\mu\nu}$:

$$\text{Re } L_{\mu\nu}(\omega) = D_{\mu\nu} \delta(\omega) + L_{\mu\nu}^{\text{reg}}(\omega). \quad (11)$$

We refer to the total weight in the diagonal coefficients as $I_{0,\mu\mu}$

and refer to the literature for the sum rules^{106,107}.

III. EXACT DIAGONALIZATION

A. Spectral representations

In the numerical analysis, we work with standard spectral representations of Eq. (10), given by:

$$D_{\mu\nu} = \frac{\pi \beta^{r+1}}{ZN} \sum_{\substack{n,o \\ E_n = E_o}} e^{-\beta E_n} \langle n | j_\mu | o \rangle \langle o | j_\nu | n \rangle, \quad (12)$$

$$L_{\mu\nu}^{\text{reg}}(\omega) = \frac{\pi \beta^r}{ZN} \frac{1 - e^{-\beta \omega}}{\omega} \sum_{\substack{n,o \\ E_n \neq E_o}} e^{-\beta E_n} \times \langle n | j_\mu | o \rangle \langle o | j_\nu | n \rangle \delta(\omega - \Delta E), \quad (13)$$

where $\Delta E = E_o - E_n$.

Since the model is nonintegrable, we expect that all Drude weights vanish for $N \rightarrow \infty$ ^{58,62,81–83}. Our main interest is in the dc limit, i.e.,

$$L_{\mu\nu} = \lim_{\omega \rightarrow 0} L_{\mu\nu}^{\text{reg}}(\omega). \quad (14)$$

For the small system sizes accessible to our analysis, most of the spectral weight is still in the Drude weights which is especially true for the quantum phases just below and above the saturation field. Since it is notoriously difficult to extract dc conductivities from finite-size data at low temperatures, we will base our analysis on two quantities, the Drude weights and integrals of $\text{Re } L_{\mu\nu}(\omega)$ over a low-frequency window. These quantities provide useful measures of the low-frequency behavior⁸⁷, and we expect that as N increases, the contribution from the Drude weight moves to finite but small frequencies. Note that this approach does not necessarily give quantities that are directly proportional to the respective dc conductivities. To simplify the notation, we will use subindices E, th, S for the energy, thermal and spin-current related quantities, respectively, and suppress double indices in the diagonal coefficients, e.g., $L_{SS} \rightarrow L_S$.

Whenever there is a coupling between the energy and the spin current, then the thermal conductivity has a magnetothermal contribution^{66,86} and the Drude weight K_{th} related to the thermal conductivity $\langle j_{th} \rangle = -\kappa \nabla T$, measured under the condition of a vanishing spin-current flow $\langle j_S \rangle = 0$, is¹⁰⁶:

$$K_{th} = D_E - \beta \frac{D_{ES}^2}{D_S}. \quad (15)$$

In Eq. (15), D_E , D_S , and D_{ES} are the Drude weights related to the coefficients that result from using the spin current j_S and the energy current j_E to set up the formalism, instead of j_{th} and j_S as above. In our numerical analysis, we, in fact, compute these expressions instead of working with the $L_{\mu\nu}$ introduced in Eq. (10). The Drude weights K_{th} can then be obtained from D_E , D_S and D_{ES} via Eq. (15).

By $I_{E[S]}(\omega)$, we denote the integral over the low-frequency

portion of the real parts of the energy and spin conductivity (up to a frequency ω), while $I_{\text{E[S]}}^0$ are the total weights:

$$I_{\text{E[S]}}(\omega) = \int_{-\omega}^{\omega} d\omega' \text{Re} L_{\text{E[S]}}^{\text{reg}}(\omega'), \quad (16)$$

$$I_{\text{E[S]}}^0 = \lim_{\omega \rightarrow \infty} I_{\text{E[S]}}(\omega). \quad (17)$$

For completeness, we provide a list of spectral representations for the Drude weights D_{E} , D_{S} and D_{ES} , as well as the regular parts of the corresponding conductivities $L_{\text{E}}^{\text{reg}}(\omega)$, $L_{\text{S}}^{\text{reg}}(\omega)$, and $L_{\text{ES}}^{\text{reg}}(\omega)$. These are the quantities that are directly obtained from our numerical procedures:

$$D_{\text{E}} = \frac{\pi\beta^2}{ZN} \sum_{\substack{n,o \\ E_n=E_o}} e^{-\beta E_n} |\langle n | j_{\text{E}} | o \rangle|^2, \quad (18)$$

$$D_{\text{S}} = \frac{\pi\beta}{ZN} \sum_{\substack{n,o \\ E_n=E_o}} e^{-\beta E_n} |\langle n | j_{\text{S}} | o \rangle|^2, \quad (19)$$

$$D_{\text{ES}} = \frac{\pi\beta}{ZN} \sum_{\substack{n,o \\ E_n=E_o}} e^{-\beta E_n} \langle n | j_{\text{E}} | o \rangle \langle o | j_{\text{S}} | n \rangle \quad (20)$$

and

$$L_{\text{E}}^{\text{reg}}(\omega) = \frac{\pi\beta}{ZN} \frac{1 - e^{-\beta\omega}}{\omega} \sum_{\substack{n,o \\ E_n \neq E_o}} e^{-\beta E_n} |\langle n | j_{\text{E}} | o \rangle|^2 \delta(\omega - \Delta E), \quad (21)$$

$$L_{\text{S}}^{\text{reg}}(\omega) = \frac{\pi}{ZN} \frac{1 - e^{-\beta\omega}}{\omega} \sum_{\substack{n,o \\ E_n \neq E_o}} e^{-\beta E_n} |\langle n | j_{\text{S}} | o \rangle|^2 \delta(\omega - \Delta E), \quad (22)$$

$$L_{\text{ES}}^{\text{reg}}(\omega) = \frac{\pi}{ZN} \frac{1 - e^{-\beta\omega}}{\omega} \sum_{\substack{n,o \\ E_n \neq E_o}} e^{-\beta E_n} \langle n | j_{\text{E}} | o \rangle \langle o | j_{\text{S}} | n \rangle \delta(\omega - \Delta E), \quad (23)$$

where again $\Delta E = E_o - E_n$.

B. Analysis of the low-frequency behavior

We start our discussion by considering the example of D_{E} and the associated integrated spectral weight $I_{\text{E}}(\omega)$. In order to compute $I_{\text{E}}(\omega)$, we choose a cut-off of $\omega = 0.5J$, which separates low- from high-frequency contributions in the regular part in the phases just below saturation. Figure 3(a) shows $I_{\text{E}}(\omega = 0.5J)/I_{\text{E}}^0$ as a function of magnetic field B and frustration α at a low temperature $T = 0.1J$. First of all, we see that the gapless phases (TLL1, TLL2, VC and SDW_2) and the fully polarized phase generally exhibit a larger low-frequency weight than the gapped phases (D and P), as expected. The SDW_2 phase exhibits significant fluctuations when crossed from small to large values of B at a fixed value of α , which can be traced back to finite-size effects.

Our main interest is in the region just below saturation: there, $I_{\text{E}}(\omega = 0.5J) \sim O(I_{\text{E}}^0)$, i.e., practically all the weight

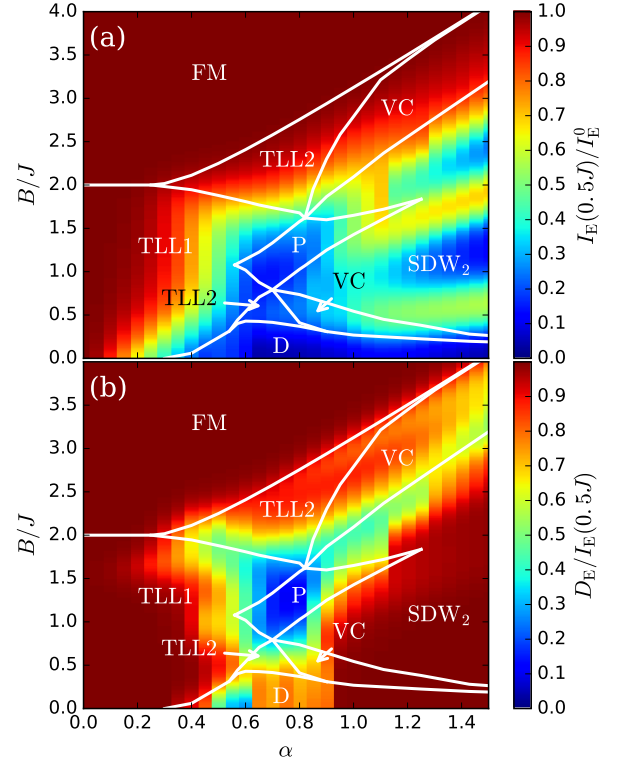


FIG. 3. (Color online) (a) Low-frequency weight $I_{\text{E}}(\omega)$ of the energy conductivity integrated up to $\omega/J = 0.5$ [see Eq. (16)] relative to the total weight in the energy conductivity I_{E}^0 [Eq. (17)] in the B - α -plane. (b) Energy Drude weight D_{E} relative to the low-frequency weight $I_{\text{E}}(\omega)$ integrated up to $\omega/J = 0.5$ [see Eq. (16)], plotted in the B - α -plane. System size $N = 20$, temperature $T/J = 0.1$, solid white lines are the $T = 0$ phase boundaries from Ref. 19.

is concentrated in the low-frequency window. The same is true in the FM phase, which at low temperatures has a very low density of excitations and can be viewed as practically noninteracting (see the discussion in Sec. IV). In the vicinity of $\alpha = 0$, i.e., the integrable Heisenberg chain, which has no finite-frequency contributions, obviously $D_{\text{E}} = I_{\text{E}}^0$. Moreover, frustration breaks this conservation law only weakly at small α and therefore, the Drude weight remains substantial in the entire TLL1 phase on small systems^{58,84}. Note that such a behavior, i.e., a large and almost system-size independent Drude weight in a nonintegrable model at low temperatures was also observed for a spin-1 chain in a magnetic field¹⁰⁸. The magnetic field induces a transition into a gapless phase for which an effective spin-1/2 XXZ chain Hamiltonian can be derived. The latter is integrable, reflected in the large finite-size Drude weights.

We next argue that at the small systems accessible to us and for the low temperatures that are relevant for a comparison to the low-energy theory developed in Sec. IV, most of the spectral weight that exists at low frequencies is concentrated in the Drude weight. To establish that notion, we plot $D_{\text{E}}/I_{\text{E}}(\omega = 0.5J)$ in Fig. 3(b). Clearly, the Drude weight accounts for most of the low-frequency spectral weight in all gapless phases, including the phases below saturation where

$D_E \gtrsim 0.8I_E(\omega = 0.5J)$. We therefore focus the following discussion on the Drude weights as a qualitative measure of the B - and α -dependence of the low-frequency part of the relevant conductivities at low temperatures.

Finally, let us comment on the temperature dependence (data not shown here). Generally, increasing temperature smoothens out the features seen in Fig. 3 yet the general trend, i.e., an enhanced weight in the thermal conductivity below the saturation field can be observed at higher temperatures as well.

C. Exact diagonalization with twisted boundary conditions

In order to reduce undesirable finite-size effects, most of the ED results shown in this work are obtained by using twisted boundary conditions (ED[ϕ]). The resulting Hamiltonian is:

$$\mathcal{H} = J \sum_{i=1}^N \left[\frac{1}{2} (e^{i\phi/N} S_i^+ S_{i+1}^- + h.c.) + S_i^z S_{i+1}^z \right] + \alpha \left\{ \frac{1}{2} (e^{i2\phi/N} S_i^+ S_{i+2}^- + h.c.) + S_i^z S_{i+2}^z \right\} - B S_i^z. \quad (24)$$

We take the average over ten different values of the twist angle ($\phi = n2\pi/10$ with $0 \leq n < 10$). Averaging over the twisted boundary conditions is known to reduce the finite-size effects for quadratic Hamiltonians⁸⁵ and we expect a similar improvement in our case.

As an example, we show a comparison between exact diagonalization with periodic boundary conditions (ED) and flux-averaged data (ED[ϕ]) in Fig. 4. There, we plot K_{th} as a function of α for $M = 0.4$ at $T = 0.1J$. It is obvious from the figure that the bare ED data suffers from large fluctuations for $\alpha > 0.6$ (compare the sets for $N = 16$ and $N = 18$), while the flux-averaged data are very close to each other for $\alpha < 1.2$. We emphasize that the main effect of the twist averaging is that fluctuations from system size to system size get reduced in some quantum phases and therefore, the convergence of the results is faster. However, in other phases fluctuations remain large (e.g., in the SDW₂ phase). This qualitative effect of flux averaging, namely the reduction of strong finite-size oscillations, is also seen in other quantities (e.g., D_E). Therefore, and for consistency reasons, we will only show data averaged over different twist angles from here on unless stated otherwise.

IV. DILUTE GAS OF FERMIONS

A. General formalism

Near its saturation field, the magnetic system can be mapped onto a dilute gas of interacting fermions. We will consider the more general case of a spin-1/2 XXZ spin model

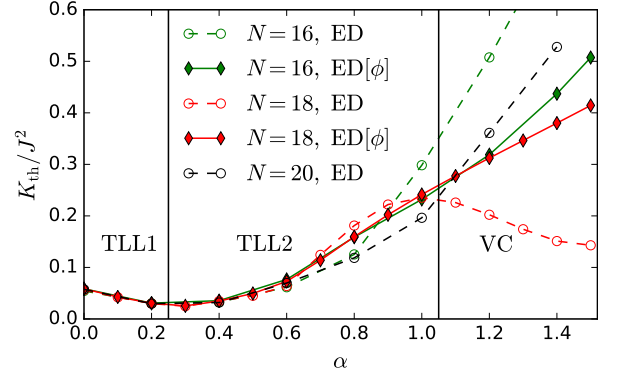


FIG. 4. (Color online) Comparison of exact diagonalization with periodic boundary conditions (ED) to results obtained from averaging over a twist angle (ED[ϕ]). K_{th} versus α at $M = 0.4$ and $T = 0.1J$ for $N = 16, 18, 20$ obtained from ED (open symbols) and $N = 16, 18$ obtained from ED[ϕ] (solid symbols). Vertical black lines are the $T = 0$ phase boundaries from Ref. 19.

that includes the Hamiltonian \mathcal{H} as a particular case:

$$\begin{aligned} \mathcal{H}^{\text{xxz}} = & J \sum_j (\Delta S_j^z S_{j+1}^z + S_j^x S_{j+1}^x + S_j^y S_{j+1}^y) \\ & + \alpha J \sum_j (\Delta S_j^z S_{j+2}^z + S_j^x S_{j+2}^x + S_j^y S_{j+2}^y) \\ & - B \sum_j S_j^z. \end{aligned} \quad (25)$$

In the following we assume $J > 0, \alpha > 0$, i.e., both exchange interactions are antiferromagnetic. The spin Hamiltonian can be mapped into a spinless-fermion model via the Jordan-Wigner transformation. In momentum space,

$$\mathcal{H}^{\text{xxz}} = \sum_k \epsilon_k c_k^\dagger c_k + \frac{1}{2!2!N} \sum_{K,k,p} \Gamma_K(p,k) c_{\frac{K}{2}-k}^\dagger c_{\frac{K}{2}+k}^\dagger c_{\frac{K}{2}+p} c_{\frac{K}{2}-p}, \quad (26)$$

where

$$\epsilon_k = J \cos k + \alpha J \cos(2k) - (B + J\Delta + \alpha J\Delta), \quad (27)$$

is the single-particle dispersion and $\Gamma_K(p,k)$ is the anti-symmetrized interaction vertex given in Appendix A. The interaction between fermions is repulsive because of the antiferromagnetic character of both exchange couplings. The single-particle dispersion ϵ_k has two minima at $\pm Q$ [$Q = \cos^{-1}(-1/4\alpha)$] when $\alpha > 1/4$. Otherwise, it has a single minimum at $Q = \pi$.

In the long-wavelength limit, we can expand the single-particle dispersion around Q and $-Q$. Given that there are two minima, we must introduce an index $\sigma = \pm$ to distinguish the particles with momenta near each of these minima. The

resulting effective Hamiltonian is:

$$\begin{aligned}\tilde{\mathcal{H}}^{\text{xxz}} = & \sum_{q,\sigma} \left(\frac{q^2}{2m^*} - \mu \right) a_{q\sigma}^\dagger a_{q\sigma} \\ & + \frac{1}{N} \sum_{\sigma,k,p} \tilde{V}_{\sigma,\sigma}(k,p) a_{-k\sigma}^\dagger a_{k\sigma}^\dagger a_{p\sigma} a_{-p\sigma} \\ & + \frac{1}{N} \sum_{\sigma,k,p} \tilde{V}_{\sigma,\bar{\sigma}}(k,p) a_{-k\sigma}^\dagger a_{k\bar{\sigma}}^\dagger a_{p\bar{\sigma}} a_{-p\sigma},\end{aligned}\quad (28)$$

where $\bar{\sigma} \equiv -\sigma$, $\mu = B_{\text{sat}} - B$ and the asymptotic behavior of the effective interaction vertex in the low-density limit $\rho = 1/N \sum_{q,\sigma} \langle a_{q\sigma}^\dagger a_{q\sigma} \rangle \ll 1$ [the momenta $p, k \leq k_F$ with p, k are defined with respect to $\pm Q$ depending on $\sigma = +$ or $-$ and $k_F = O(\rho)$] is given by

$$\begin{aligned}\tilde{V}_{\sigma,\sigma}(k,p) = \tilde{V}_{\bar{\sigma},\bar{\sigma}}(k,p) &= C(Q)pk + O(\rho^3), \\ \tilde{V}_{\sigma,\bar{\sigma}}(k,p) = \tilde{V}_{\bar{\sigma},\sigma}(k,p) &= \frac{\pi\Lambda_0}{m^* f\left(\frac{2\Lambda_0}{p+k}\right)} - \left(\frac{\pi\Lambda_0}{m^* f\left(\frac{2\Lambda_0}{p+k}\right)} \right)^2 \frac{D_2(Q)}{D_1(Q)} \\ &+ \frac{4 \sin^6(Q)}{D_1} pk + O(\rho^3).\end{aligned}\quad (29)$$

These effective interaction vertices are obtained by summing up series of ladder diagrams, as described in the Appendix A. $\Lambda_0 \sim \pi\rho/2$ is the infrared cutoff introduced to regularize the integrals that determine the effective interaction vertices and $C(Q)$, $D_1(Q)$ and $D_2(Q)$ are functions that can be found in the Appendix A.

In the following, we are going to assume that B approaches B_{sat} from above ($\mu < 0$, see Fig. 5) and compute the ground-state energy in the subspace with fixed but infinitesimally small density ρ (note that the global ground state is the empty state $\rho = 0$ for $\mu < 0$). The ground state in the finite-density sector will allow us to determine when the chiral susceptibility becomes divergent for $\mu \rightarrow 0$ (see Fig. 5). After a mean-field (MF) decoupling of the interaction term, we can compute the energy density,

$$e = e_{\text{kin}} + e_{\text{int}} - \mu\rho, \quad (30)$$

as a function of the difference between the fermionic densities ρ_{+Q} and ρ_{-Q} , with

$$\rho_{\sigma Q} = \int \langle a_{k\sigma}^\dagger a_{k\sigma} \rangle \frac{dk}{2\pi}. \quad (31)$$

The total fermionic density is $\rho = \rho_{+Q} + \rho_{-Q}$.

The contribution from the kinetic energy term is:

$$e_{\text{kin}} = \frac{\pi^2 \rho_{+Q}^3}{6m^*} + \frac{\pi^2 \rho_{-Q}^3}{6m^*} = \frac{\pi^2}{6m^*} \left[\frac{\rho^3}{4} + 3\rho\delta^2 \right], \quad (32)$$

where $\rho_{\sigma Q} = \rho/2 + \sigma\delta$ and $-\rho \leq 2\delta \leq \rho$ is the difference between the fermion density around the Q and $-Q$ points, i.e., the order parameter of the chiral phase. The contribution from the interaction terms, e_{int} , can be expanded in powers of ρ . The leading-order contribution (order ρ^3) up to quadratic or-

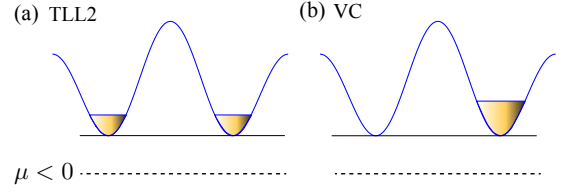


FIG. 5. (Color online) Single-particle dispersion with two minima. (a) $\rho_{+Q} = \rho_{-Q}$; (b) $\rho_{+Q} = \rho$ and $\rho_{-Q} = 0$. The chemical potential is assumed to be negative $\mu < 0$ (namely above the saturation field B_{sat}), and we consider the subspace with a fixed density $\rho = \rho_{+Q} + \rho_{-Q}$ (excited states).

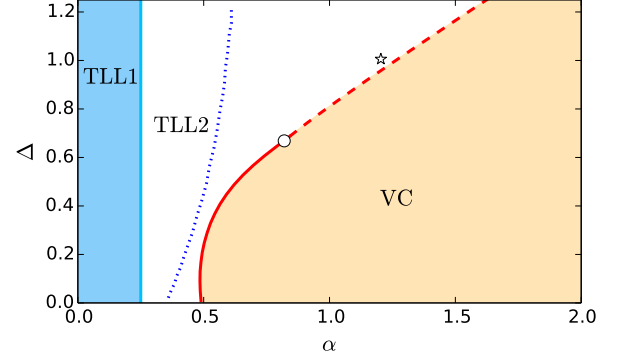


FIG. 6. (Color online) Phase diagram in the Δ - α -plane, where Δ is the spin-exchange anisotropy (the isotropic case corresponds to $\Delta = 1$) and $\alpha = J_2/J_1$. The red line is the phase boundary obtained from the dilute Fermi-gas approach, where the dashed part is first order while the solid part is second order, the black pentagram is the numerical result from Ref. 19. The dotted line is the phase boundary obtained from the hard-core boson approach^{27,32}. For $\alpha < 0.25$, the ground state becomes a TLL1 phase irrespective of Δ .

der in δ is:

$$e_{\text{int}}^{(1)} = \frac{\pi^2}{8m^*} \bar{\Lambda}_0 \Phi\left(\bar{\Lambda}_0, \frac{2\delta}{\rho}\right) (\rho^3 - 4\rho\delta^2), \quad (33)$$

where $\bar{\Lambda}_0 = \Lambda/k_F$ with $k_F = \pi\rho/2$. The infrared cut-off must be chosen so that $e_{\text{kin}} + e_{\text{int}}^{(1)}$ is independent of δ for the phase transition to take place at a given value of $\alpha > 1/4$ ³². The phase-transition line $\alpha_c(\Delta)$ is then determined by the $O(\rho^4)$ corrections, arising from subleading contributions (order ρ^2) to the interaction vertex.

Up to an irrelevant constant, the expansion of the energy density up to fourth order in ρ is

$$\begin{aligned}e_{\text{int}}^{(2)} = & g\rho^2\rho_{-Q}\rho_{+Q} + u(\rho_{-Q}^3\rho_{+Q} + \rho_{-Q}\rho_{+Q}^3) \\ & + w(\rho_{+Q}^4 + \rho_{-Q}^4),\end{aligned}\quad (34)$$

where the first line corresponds to the interaction between fermions from different minima ($\pm Q$) and the second line corresponds to the interaction between fermions from the same minimum. The coefficients g , u and w are derived in Appendix A. The expansion of the total energy density (30) in

powers of the order parameter δ becomes

$$f_{\text{tot}}(\delta) = f_{\text{tot}}(\delta = 0) + A\rho^2\delta^2 + B\delta^4 - \mu\rho, \quad (35)$$

the minimization of which with respect to δ determines the phase boundary between the TLL2 and VC phases, namely the function $\alpha_c(\Delta)$ presented in Fig. 6 on the $\Delta - \alpha$ plane (see Appendix A for more details, where the coefficients of this expansion are also given). In the spin language, the broken-symmetry state (VC) corresponds to the chiral state with order parameter $\kappa_{ij}^{\text{vc}} \neq 0$. The nature of the transition changes from first to second order at a critical value of the anisotropy $\Delta_c \simeq 0.6684$. For isotropic spin exchange, the transition turns out to be weakly first order and the critical value of α , $\alpha_c(\Delta = 1) \simeq 1.264$, is in very good agreement with the numerical results of Ref. 19 (the dotted line in Fig. 6 indicates the phase boundary obtained in Fig. 1 by solving the two-body problem in the bosonic language). We note that the bosonic treatment presented in Refs. 27 and 32 (which was primarily developed for frustrated spin chains with $S > 1/2$) gives a critical value of α which is rather far from the numerical result, as already pointed out in Ref. 27. We attribute this difference between the bosonic and fermionic treatments of the problem to the fact that the mean-field approximation of the low-energy Hamiltonian \tilde{H}^{xxz} is better justified in the fermionic case. The quantum critical point at the saturation field is a free-fermion fixed point for $S = 1/2$ (the Fermi exclusion principle accounts exactly for the hard-core constraint)¹⁰⁹. We also note that in one dimension, the exact solution of the two-body problem does not necessarily provide accurate values of the coefficients A and B (the value of this coefficients is modified by n -body processes with $n > 2$).

An important consequence of this derivation is that the renormalization of the bare single-particle dispersion,

$$\epsilon_k(\alpha) = J(\cos k + \alpha \cos 2k - \cos Q - \alpha \cos 2Q) + (B - B_{\text{sat}}), \quad (36)$$

is quadratic in the fermion density. In particular, this implies that the single-particle dispersion is not renormalized at all for $B > B_{\text{sat}}$ and $T = 0$. This is a direct consequence of the U(1) invariance of the model, which leads to a dynamical exponent $z = 2$ (quadratic dispersion) at $B = B_{\text{sat}}$. Given that $\rho \propto \sqrt{B_{\text{sat}} - B}$, for $B \lesssim B_{\text{sat}}$, the correction to the Fermi velocity is proportional to $m^*(B_{\text{sat}} - B)$, while the bare Fermi velocity is of order $\sqrt{(B_{\text{sat}} - B)}$. Consequently, the single-mode dispersion is well approximated by the bare dispersion (36) for $B \lesssim B_{\text{sat}}$. This simple observation enables an accurate calculation of $K_{\text{th}} \propto vT$ (for $T \ll |B - B_{\text{sat}}|$) in this regime because it only depends on the velocity $v \simeq \partial\epsilon_k/\partial k|_{k_F} = |k_F - Q|/m^*$ of the low-energy modes (note that the same is not true for the low T behavior of $D_{\text{th}} \propto Kv/T$, which also depends on the value of the Luttinger parameter K^{86}). At $T \simeq B - B_{\text{sat}}$, K_{th} crosses over into the $K_{\text{th}} \propto T^{3/2}/\sqrt{m^*}$ behavior that is obtained at the fixed point $B = B_{\text{sat}}$. Finally, for $B > B_{\text{sat}}$, we have $K_{\text{th}} \propto T^{3/2}e^{-\Delta/T}/\sqrt{m^*}$. We note that in the three regimes K_{th} has the same dependence on T and m^* as $C_V\langle v^2 \rangle$, where $\langle v^2 \rangle$ is the average value of the square of the quasiparticle velocity.

An important observation is that the behavior of K_{th} is dic-

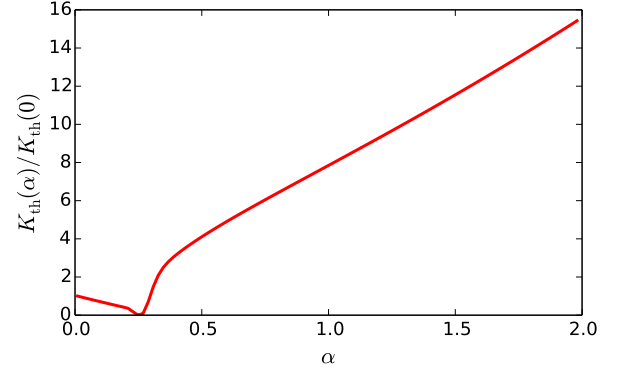


FIG. 7. (Color online) Drude weight of the thermal conductivity as a function of α for the non-interacting fermionic theory arising from a mean-field decoupling of \tilde{H}^{xxz} . The fermionic density is fixed at $\rho = M_{\text{sat}} - M = 0.01$ and $T = 8E_F(\alpha = 0)$, where $E_F(\alpha = 0)$ is the Fermi energy at $\alpha = 0$.

tated by the single-mode dispersion, which is very well approximated by the bare dispersion (36) near the saturation field because corrections to the Fermi velocity are of order ρ^2 . From the viewpoint of K_{th} , the main difference between the TLL2 and the (chiral) TLL1 is that the former has two channels of energy carriers, while the latter has only one. Nevertheless, at the bare level, the Fermi velocity of carriers in the TLL2 ($v = \pi\rho/2m^*$) is twice smaller than the Fermi velocity $v = \pi\rho/m^*$ of carriers in the TLL1 (this is a direct consequence of the quadratic dispersion around $\pm Q$). Consequently, the factors of 2 compensate to give $K_{\text{th}} \propto \pi\rho/m^*$ in both phases. Based on the above considerations, the dependence of K_{th} on α right below the saturation field and at a fixed magnetization value $M \lesssim M_{\text{sat}}$ should be very similar to the one shown in Fig. 7, which is obtained using the non-interacting fermionic theory arising from a mean field decoupling of \tilde{H}^{xxz} in Eq. (28) (see also the discussion in the Sec. V A). As anticipated in the introduction, the α -dependence of K_{th} has the same trend as the α -dependence of $1/m^*$ shown in Fig. 2.

V. RESULTS FROM EXACT DIAGONALIZATION

In this section, we complement our preceding analytical arguments by a numerical study of the transport coefficients of our model in finite magnetic fields. We first present a direct comparison between our dilute Fermi-gas theory and exact diagonalization in Sec. V A. Then, we proceed to comparing D_E and K_{th} in order to assess the significance of magnetothermal corrections in Sec. V B. In Sec. V C, we compare the dependence on α at low and high magnetizations.

A. Comparison of dilute fermion theory to exact diagonalization for $B > B_{\text{sat}}$

In the previous section we argued that a MF decoupling of \tilde{H}^{xxz} should give quantitatively correct results in the small

density limit for the Drude weights introduced in Sec. II. In particular, the fermionic density is very small above the saturation field ($B > B_{\text{sat}}$) for $T \ll B - B_{\text{sat}}$ (exponentially small in $B - B_{\text{sat}}/T$). The purpose of this subsection is to verify this statement by comparing the analytical treatment with exact-diagonalization results. Under the mean-field description of $\tilde{\mathcal{H}}^{\text{xxz}}$, the thermal and spin current operators are simply given by

$$j_{\text{th}}^{\text{MF}} = \sum_k \epsilon_k v_k n_k, \quad j_S^{\text{MF}} = \sum_k v_k n_k, \quad (37)$$

where $v_k = \partial \epsilon_k / \partial k$ is the group velocity and $n_k = c_k^\dagger c_k$ is the fermionic particle number. Within the mean-field approximation, the spin/energy-current correlation functions have only a singular contribution at zero frequency [see Eq. (11)], with the Drude weights given by:

$$\begin{aligned} D_{\text{EE}} &= -\frac{\beta}{2} \int_0^{2\pi} (\epsilon_k v_k)^2 \partial_{\epsilon_k} f(\epsilon_k) dk, \\ D_{\text{ES}} &= -\frac{1}{2} \int_0^{2\pi} \epsilon_k v_k^2 \partial_{\epsilon_k} f(\epsilon_k) dk, \\ D_{\text{SS}} &= -\frac{1}{2} \int_0^{2\pi} v_k^2 \partial_{\epsilon_k} f(\epsilon_k) dk, \end{aligned} \quad (38)$$

where $f(\epsilon_k) = 1/[1 + \exp(\beta \epsilon_k)]$ is the Fermi function. The single-particle dispersion around each minimum at $k = \pm Q$ is $\epsilon_k = \Delta_g + \frac{k^2}{2m^*}$, with $\Delta_g = B - B_{\text{sat}} + \pi^2 \rho^2 / 4m^*$. For $T \ll \Delta_g$, we have

$$\begin{aligned} D_{\text{EE}} &\simeq \frac{4\Delta_g^2}{\sqrt{2m^*T}} e^{-\beta \Delta_g} \Gamma\left(\frac{3}{2}\right), \\ D_{\text{ES}} &\simeq \frac{4\Delta_g \sqrt{T}}{\sqrt{2m^*}} e^{-\beta \Delta_g} \Gamma\left(\frac{3}{2}\right), \\ D_{\text{SS}} &\simeq \frac{4\sqrt{T}}{\sqrt{2m^*}} e^{-\beta \Delta_g} \Gamma\left(\frac{3}{2}\right). \end{aligned} \quad (39)$$

Under the condition of a vanishing spin-current flow, the thermal conductivity K_{th} is computed by substituting these expressions into Eq. (15). For $T \ll \Delta_g$, we get

$$K_{\text{th}} = \frac{4T^{3/2}}{\sqrt{2m^*}} e^{-\beta \Delta_g} \Gamma\left(\frac{7}{2}\right) \quad (40)$$

where $\Gamma(x)$ is the Gamma function.

We note that $K_{\text{th}} \propto 1/\sqrt{m^*}$ for $B > B_{\text{sat}}$, while $K_{\text{th}} \propto 1/m^*$ for $B \lesssim B_{\text{sat}}$, implying that the increase of K_{th} as a function of α is much more pronounced in the TLL regime, as it is evident from direct comparison between Figs. 7 and 8. Figure 8 also shows a comparison with the results obtained from exact diagonalization (ED[ϕ]) in the high-field regime $B > B_{\text{sat}}$. We fix the magnetic field at $B = B_{\text{sat}} + 0.2J$ and choose a temperature $T/J = 0.1$, which is half of the spin gap $\Delta_g = 0.2J$. Given that the low-energy sector of \mathcal{H} is well described by an effective non-interacting theory, we expect that the averaging over the twist angle should drastically reduce the finite-size effects. Indeed, the $N = 16$ and $N = 18$ ED[ϕ] data are very

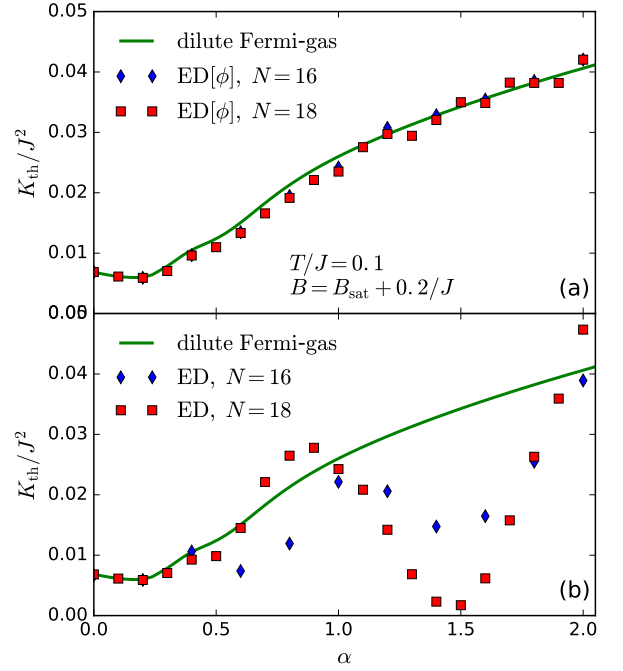


FIG. 8. (Color online) K_{th} as defined in Eq. (15) at magnetic field $B = B_{\text{sat}} + 0.2/J$ as a function of α at $T/J = 0.1$. The solid green line is the dilute Fermi-gas result and the different symbols are exact-diagonalization results for system sizes $N = 16$ (blue diamonds) and $N = 18$ (red squares). (a) ED[ϕ] obtained by averaging over 10 different values of the twist angle as explained in Sec. V A, (b) ED without average over twist angles.

similar, and, as shown in Fig. 8(a), the analytical results are in excellent agreement with ED[ϕ]. At this point, where we have analytical data available for comparison, we can further illustrate the effect of the averaging over twist angles. In Fig. 8(b), we present non averaged data which for $\alpha \gtrsim 0.4$ fluctuates wildly. Comparing Fig. 8(a) to Fig. 8(b) it is evident that the averaging over twist angles leads to a remarkable improvement of the results.

B. Magnetothermal corrections

The reason for focussing on D_E and K_{th} is that their difference is directly related to the magnetothermal corrections due to a field-induced coupling of the spin and the energy current. Figures 9(a) and (b) thus also illustrate the magnitude and qualitative field dependence introduced by the second term in Eq. (15). As a function of B , D_E first increases and then takes a maximum in the high-field vector-chiral phase before decreasing upon entering into the (gapped) fully polarized region. The maximum of D_E in the VC phase is likely not a sole consequence of vector chirality, since such a maximum is also present in the field-induced Luttinger liquid phase in the spin-1/2 XXZ chain⁸⁶ and is thus a consequence of the proximity to the fully-polarized phase. The thermal Drude weight K_{th} exhibits a different field dependence: apart from finite-size fluctuations in the SDW₂ phase, K_{th} is a monotonously decreasing

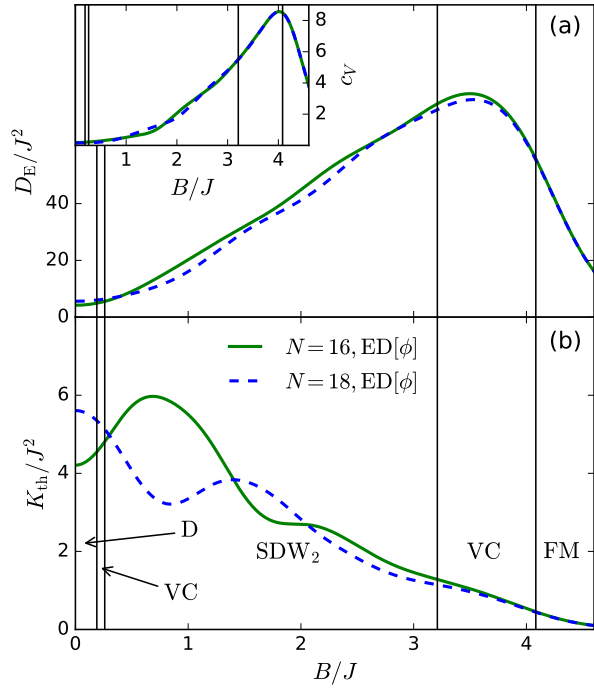


FIG. 9. (Color online) (a) Energy Drude weight D_E and (b) thermal Drude weight K_{th} [see Eq. (15)] as a function of the magnetic field B at $\alpha = 1.5$ for system sizes $N = 16, 18$ at $T/J = 0.25$. Vertical black lines are the $T = 0$ phase boundaries from Ref. 19. Inset of (a): Specific heat $c_V = C_V/N$ at $\alpha = 1.5$ for system sizes $N = 16, 18$ at $T/J = 0.25$. All data were obtained by averaging over 10 different values of the twist angle as explained in Sec. V A.

function of B . Magnetothermal corrections result in a significant reduction of the absolute values, i.e., $K_{th} < D_E$. This difference in the field dependence of D_E and K_{th} resembles the behavior known for the spin-1/2 XXZ chain in its partially polarized Luttinger-liquid phase⁸⁶.

It is further very instructive to contrast the field-dependencies of D_E and K_{th} to the specific heat, which is shown in the inset of Fig. 9(a) (see Refs. 29, 31, 110–112 for previous studies of the specific heat in this model). The specific heat increases rapidly as a function of magnetic field and also takes a maximum in the vicinity of the high-field vector-chiral phase and thus behaves similarly to the energy-current Drude weight D_E but very differently from the full thermal Drude weight K_{th} that includes magnetothermal corrections. This can be understood by recalling that K_{th} has the same temperature and mass dependence as $C_V \langle v^2 \rangle$. For a fixed temperature, C_V is maximized at the saturation field because the dispersion relation becomes quadratic at $B = B_{sat}$. In other words, at low enough temperature: $C_V \propto m^* T / \sqrt{B_{sat} - B}$ for $B \lesssim B_{sat}$ and $T \ll (B_{sat} - B)$, $C_V \propto \sqrt{m^* T}$ at $B = B_{sat}$ and $C_V \propto \sqrt{m^* T} e^{-\Delta_g/k_B T}$ for $B > B_{sat}$. However, K_{th} is not maximized at $B = B_{sat}$ because $\langle v^2 \rangle$ is suppressed upon approaching the saturation field: $\langle v^2 \rangle \propto (B_{sat} - B)/(m^*)^2$ for $B \lesssim B_{sat}$, $\langle v^2 \rangle \propto T/m^*$ at $B = B_{sat}$ and $\langle v^2 \rangle \propto T e^{-\Delta_g/k_B T}/m^*$ for $B > B_{sat}$. As a result, we have that $K_{th} \propto \sqrt{B_{sat} - B} T/m^*$ for $B \lesssim B_{sat}$ and $T \ll (B_{sat} - B)$, $K_{th} \propto T^{3/2}/\sqrt{m^*}$ at $B = B_{sat}$ and

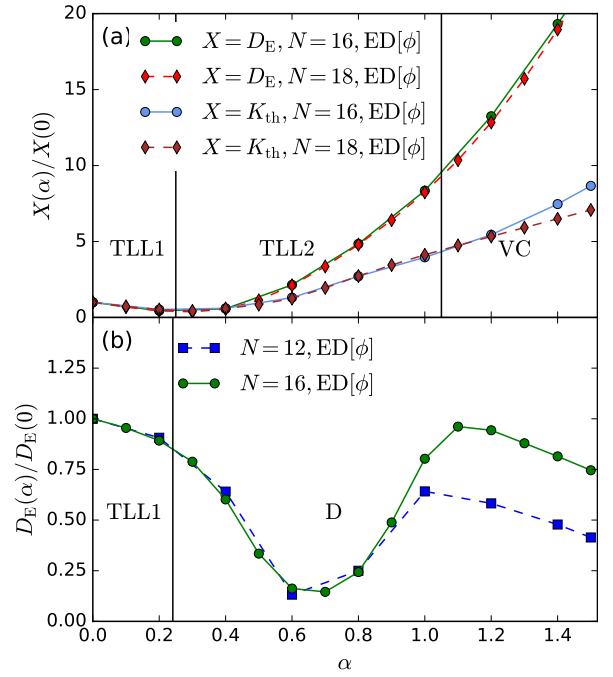


FIG. 10. (Color online) Energy Drude weight D_E and K_{th} as defined in Eq. (15) at magnetization (a) $M = 0.4$ and (b) $M = 0$ for $T/J = 0.1$ as a function of α . In (a), we show data for system sizes $N = 16$ and $N = 18$ (solid and dashed lines respectively). In (b), only D_E is shown for $N = 12$ and $N = 16$ (dashed and solid lines respectively) since $D_E = K_{th}$ at $B = 0$. All quantities are obtained by averaging over 10 different twist angles and normalized to their values at $\alpha = 0$. Vertical black lines are the $T = 0$ phase boundaries at the corresponding field strength B from Ref. 19.

$K_{th} \propto T^{3/2} e^{-\Delta_g/k_B T} / \sqrt{m^*}$ for $B > B_{sat}$, implying that K_{th} must decrease upon approaching the saturation field, as shown in Fig. 9(b). Therefore, these qualitatively different field dependencies may allow one to detect or rule out magnetothermal corrections in quasi-one-dimensional quantum magnets (see Refs. 89 and 101 for experimental studies along those lines).

C. Dependence on frustration α at high- versus small magnetization

The final result of our work that further supports the dilute Fermi-gas arguments of Sec. IV is presented in Fig. 10(a). There, we plot the Drude weights D_E and K_{th} as a function of α at a fixed magnetization of $M = 0.4$ and at $T/J = 0.1$, normalized to their respective values at $\alpha = 0$. For both D_E and K_{th} , we recover the prediction from dilute Fermi-gas theory, namely a significant increase of the Drude weights once α goes beyond $\alpha = 0.25$. This agreement between the exact diagonalization and the dilute Fermi-gas prediction concerning the α dependence of the thermal Drude weight just below saturation is a main result of our work, as it suggests an enhanced thermal conductivity upon entering the high-field vector-chiral phase.

We finally compare this to the α -dependence of the Drude

weights at small values of M for which we also presented qualitative arguments in the Introduction, Sec. I. These results are shown in Fig. 10(b) for $M = 0$ (since $D_E = K_{th}$ at $B = 0$ we only show D_E here). For this choice of T and M , the system goes first through the TLL1 phase and then enters into the dimerized phase. D_E has a pronounced minimum at $\alpha = 0.7$ before the Drude weight starts to increase again until the maximum at about $\alpha \approx 1.2$ is reached. This behavior in the dimerized phases can be understood as follows: between $\alpha \approx 0.25$ and $\alpha \approx 0.7$ the thermal conductivity decreases as the gap increases. For $\alpha > 0.7$ the gap gets smaller so one expects an increase of the thermal conductivity.

While this behavior is seen for $0.7 \lesssim \alpha \lesssim 1.2$, the thermal Drude weight decreases for even bigger α . We believe that this is a finite-size effect (which cannot be remedied by flux averaging), rooted in the fact that we work at fixed temperature.

The comparison of Fig. 10(a) and Fig. 10(b) underlines the main result of our work: at small values of M , the frustration leads to a decrease of the thermal Drude weight by a factor of ten comparing the values at $\alpha = 0$ to the minimum at $\alpha \approx 0.7$, while at large M , a pronounced increase is observed once the frustration parameter exceeds $\alpha \approx 0.25$. This numerical result supports the conclusions of the dilute Fermi-gas analysis of Sec. IV.

VI. SUMMARY AND DISCUSSION

In this work we used a combination of a dilute Fermi-gas theory and exact diagonalization to study the thermal conductivity of frustrated spin-1/2 chains in the presence of a large magnetic field. We focused on the behavior in the vicinity of the saturation field and on systems with antiferromagnetic exchange couplings. The dilute Fermi-gas theory consists of a mean-field treatment of the effective low-energy Hamiltonian that is obtained by taking the long wavelength limit of the original model. The renormalized two-body interactions are obtained by adding ladder diagrams. This mean-field treatment includes many-body effects *beyond the exact solution of the two-body problem*. Like any other mean-field approximation, it cannot reliably predict the correct order of the quantum phase transition between the TLL2 and VC phases. However, the value of α_c that is obtained from this treatment is in very good agreement with previous numerical results¹⁹, confirming that many-body effects (beyond two-body) give a significant contribution to the Landau-Ginzburg expansion of the energy in powers of the VC order parameter.

As a main result, we predict a significant increase of the low-temperature thermal Drude weight as the frustration parameter red increases. Interactions enhance this effect. By contrast, at small values of the total magnetization or low magnetic fields, turning on frustration leads to a decrease of the thermal Drude weight for sufficiently large values of the frustration parameter $\alpha \gtrsim 0.2$, with a pronounced minimum at $\alpha \approx 0.7$.

We further elucidated the role of magnetothermal corrections to thermal transport. While the increase of the ther-

mal Drude weight K_{th} in the vector-chiral phase below saturation is present in either case, the magnetic field and α dependence of K_{th} is qualitatively affected by the presence of the magnetothermal coupling. While the bare energy Drude weight increases with B with a maximum before the fully polarized phase is reached, this is not the case for the thermal Drude weight K_{th} , which shows a decrease as a function of B . These observations on the field dependence of the thermal conductivity compared to the specific heat are similar to those reported for the finite-magnetic field transport properties of spin-1/2 XXZ chains⁸⁶ and may thus be used to detect magnetothermal corrections.

Our data shows that flux-averaging can significantly reduce finite-size dependencies as we demonstrated in the high-field regime. It would be worth exploring the advantages of flux-averaging in the whole phase diagram which is beyond the scope of the present work.

Our conclusions should apply to real materials in so far as we need to assume that no drastic changes in the magnetic field dependence result from external scattering mechanisms. Investigating this point for the case of frustrated spin systems remains as an open theoretical problem. The prediction of an enhanced low-temperature low-frequency weight in the thermal conductivity should carry over to higher-dimensional frustrated spin systems as well so long as these still realize a free-fermion fixed point below saturation.

Acknowledgments: We thank C. Karrasch for his contributions in early stages of this project. This work was supported by the Deutsche Forschungsgemeinschaft (DFG, German Research Foundation) under project number 207383564 via Research Unit FOR 1807. J.S. and F.H.-M. further acknowledge support from SFB 1073 (funded by the DFG, Deutsche Forschungsgemeinschaft) at the University of Göttingen. Part of this research was conducted at KITP at UCSB. This research was supported in part by the National Science Foundation under Grant No. NSF PHY-1748958.

Appendix A: Fermionic theory

The (anti-symmetrized) vertex of Eq. (26) is

$$V_K(p, k) = \sum_{i=1}^2 A_i(K) T_i(p) T_i(k), \quad (A1)$$

where K is the center-of-mass momentum,

$$A_1(K) = 4J(\Delta + 2\alpha \cos(K)), \quad (A2)$$

$$A_2(K) = 4\alpha J\Delta \quad (A3)$$

and

$$T_1(p) = \sin p, \quad (A4)$$

$$T_2(p) = \sin 2p \quad (A5)$$

are the lattice harmonics associated with nearest and next-nearest-neighbor interactions. The scattering amplitude be-

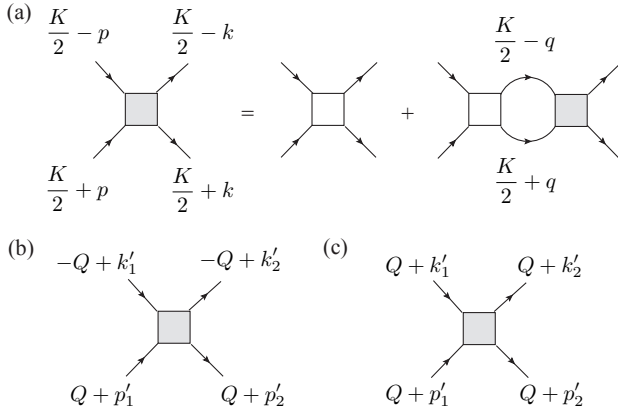


FIG. 11. (a) Ladder diagrams contributing to the effective interaction vertex. (b) Interaction vertex for two fermions from opposite minima. (c) Interaction vertex for two fermions from the same minimum.

tween fermions is strongly renormalized in the low-density limit ($\rho \ll 1$) and it is determined by the ladder diagrams depicted in Fig. 11(a), corresponding to the solution of the Bethe-Salpeter (BS) equation

$$\Gamma_{K,\Omega}(p, k) = V_K(p, k) - \frac{1}{2} \int_0^{2\pi} \frac{dq}{2\pi} \frac{V_K(p, q) \Gamma_{K,\Omega}(q, k)}{\epsilon_{\frac{K}{2}-q} + \epsilon_{\frac{K}{2}+q} - \Omega - i0^+}. \quad (\text{A6})$$

K is the center-of-mass momentum and Ω the total frequency. We consider the case with $\alpha = J_2/J_1 > 1/4$ where the non-interacting spectrum of the fermion contains two minima at $\pm Q$ related by spatial inversion symmetry. The solution is a linear combination of the lattice harmonics $T_1(p), T_2(p)$:

$$\Gamma_{K,\Omega}(p, k) = \sum_{i=1}^2 B_i(k; K, \Omega) T_i(p), \quad (\text{A7})$$

where the coefficients B_i satisfy a system of two linear equations

$$\begin{pmatrix} \frac{1}{A_1(K)} + \tau_{11} & \tau_{12} \\ \tau_{21} & \frac{1}{A_2(K)} + \tau_{22} \end{pmatrix} \begin{pmatrix} B_1(k) \\ B_2(k) \end{pmatrix} = \begin{pmatrix} T_1(k) \\ T_2(k) \end{pmatrix}, \quad (\text{A8})$$

with

$$\tau_{ij}(K, \Omega) = \frac{1}{2} \int_0^{2\pi} \frac{dq}{2\pi} \frac{T_i(q) T_j(q)}{\epsilon_{\frac{K}{2}-q} + \epsilon_{\frac{K}{2}+q} - \Omega - i0^+}. \quad (\text{A9})$$

For the construction of an effective low-energy description used in the main text, we compute the static component of the interaction vertex ($\Omega = 0$) between fermions from the same and opposite minima of the non-interacting spectrum.

1. Scattering amplitude between fermions from different minima

The scattering process depicted in Fig. 11(b) is described by the scattering amplitude

$$\Gamma_{p_1+k_1} \left(Q + \frac{p_1 - k_1}{2}, Q + \frac{p_2 - k_2}{2} \right), \quad (\text{A10})$$

where p_1, k_1 are the incoming momenta of the two fermions and p_2, k_2 are the outgoing momenta. The non-interacting kinetic energy spectrum becomes gapless at the saturation field and $\tau_{ij}(K, \Omega = 0)$ has an infrared divergence. To regularize this integral, we introduce an infrared cutoff Λ_0 obtaining

$$\tau_{ij}(K, 0) = \frac{m^*}{\pi \Lambda_0} T_i(Q) T_j(Q) f \left(\frac{2\Lambda_0}{K} \right) + \tau_{ij}^{\text{reg}}(K, 0). \quad (\text{A11})$$

The first term corresponds to the singular contribution in the infrared limit with

$$f(x) = x \left(\frac{\pi}{2} \text{sgn}(x) - \arctan(x) \right). \quad (\text{A12})$$

The second term of Eq. (A11) is the remaining regular integral. Substituting this result into the Bethe-Salpeter equation, we obtain the scattering amplitude expanded in powers of $\Lambda_0 \propto \rho \propto k_F$:

$$\Gamma_K(Q + \tilde{p}, Q + \tilde{k}) = \frac{\pi \Lambda_0}{m^* f \left(\frac{2\Lambda_0}{K} \right)} - \left(\frac{\pi \Lambda_0}{m^* f \left(\frac{2\Lambda_0}{K} \right)} \right)^2 \frac{D_2}{D_1} + \frac{4 \sin^6(Q)}{D_1} p k + \mathcal{O}(k_F^3), \quad (\text{A13})$$

where

$$D_1 = T_1^2(Q) \left(\frac{1}{A_2(0)} + \tau_{22}^{\text{reg}}(0) \right) + T_2^2(Q) \left(\frac{1}{A_1} + \tau_{11}^{\text{reg}}(0) \right) - T_1(Q) T_2(Q) \left(\tau_{21}^{\text{reg}}(0) + \tau_{12}^{\text{reg}}(0) \right) \quad (\text{A14})$$

and

$$D_2 = \left(\frac{1}{A_2} + \tau_{22}^{\text{reg}}(0) \right) \left(\frac{1}{A_1} + \tau_{11}^{\text{reg}}(0) \right) - \tau_{12}^{\text{reg}}(0) \tau_{21}^{\text{reg}}(0). \quad (\text{A15})$$

2. Scattering amplitude between fermions from the same minimum

We consider the scattering process depicted in Fig. 11(c), where the two incoming and outgoing fermions belong to the same minimum of the single-particle dispersion (either Q or $-Q$). The corresponding scattering amplitude is

$$\Gamma_{2Q+p'_1+k_1} \left(\frac{p_1 - k_1}{2}, \frac{p_2 - k_2}{2} \right). \quad (\text{A16})$$

In contrast to the previous case, the integral τ_{ij} is convergent. The expansion of this vertex up to quadratic order in momenta

gives

$$\Gamma_{2Q+\delta K}(p, k) = Cpk, \quad (\text{A17})$$

where

$$C = \frac{1}{M} \left[\left(\frac{1}{A_2(2Q)} + \tau_{22}(2Q, 0) \right) + 4 \left(\frac{1}{A_1(2Q)} + \tau_{11}(2Q, 0) \right) - 2\tau_{12}(2Q, 0) - 2\tau_{21}(2Q, 0) \right], \quad (\text{A18})$$

and

$$M = (A_1^{-1}(2Q) + \tau_{11}(2Q, 0)) (A_2^{-1}(2Q) + \tau_{22}(2Q, 0)) - \tau_{12}(2Q, 0)\tau_{21}(2Q, 0). \quad (\text{A19})$$

Given the spatial inversion symmetry of \mathcal{H}^{xz} , we also have:

$$\Gamma_{-2Q+\delta K}(p, k) = Cpk. \quad (\text{A20})$$

The effective low-energy Hamiltonian given in Eq. (28) of the main text is obtained by replacing the bare interaction vertex in Eq. (26) with the renormalized vertex obtained in this section.

3. Hartree-Fock approximation

The very small effective interaction vertex in the low-density limit justifies the application of a Hartree-Fock (HF) approximation to the effective Hamiltonian. The interaction term is approximated by

$$\mathcal{H}_{\text{int}}^{\text{HF}} = \frac{1}{2N} \sum_{K, p, q} V_{p+q} \left(\frac{q-p}{2}, \frac{q-p}{2} \right) [n_p c_p^\dagger c_q + n_q c_p^\dagger c_p - n_p n_q], \quad (\text{A21})$$

where $n_p = \langle c_p^\dagger c_p \rangle$. The first two terms renormalize the non-interacting spectrum, which is of order ρ .

To account for the competition between the two-component Tomonaga-Luttinger liquid and the vector-chiral phase, we compute the lowest energy density for a fixed density ρ as a function of the order parameter δ . The fermion density around the σQ minimum is $\rho_{\sigma Q} = \frac{\rho}{2} + \sigma\delta$ with $\sigma = \pm$. The Fermi momentum around each minimum is given by $k_F^\sigma = k_F + \sigma\Delta$, with $k_F = \frac{\pi\rho}{2}$ and $\Delta = \pi\delta$. The kinetic energy density is

$$e_{\text{kin}} = e_0 (1 + 3\bar{\delta}^2), \quad (\text{A22})$$

where $e_0 \equiv \frac{\pi^2}{24m^*} \rho^3$ is the kinetic energy density of the non-chiral phase with $\rho_{+Q} = \rho_{-Q} = \rho/2$ and $\bar{\delta} \equiv \frac{2\delta}{\rho}$ is the normalized vector-chirality order parameter. The interaction energy density is given by

$$e_{\text{int}} = \frac{1}{2} \int \frac{dp}{2\pi} \frac{dq}{2\pi} \Gamma_{p+q} \left(\frac{q-p}{2}, \frac{q-p}{2} \right) n_p n_q \equiv \sum_{\sigma\sigma'} e_{\text{int}}^{\sigma\sigma'}, \quad (\text{A23})$$

where

$$e_{\text{int}}^{++} = \frac{1}{2} \int_{-k_F^1}^{k_F^1} \frac{dp}{2\pi} \int_{-k_F^1}^{k_F^1} \frac{dq}{2\pi} \Gamma_{2Q+p+q} \left(\frac{q-p}{2}, \frac{q-p}{2} \right), \quad (\text{A24})$$

$$e_{\text{int}}^{--} = \frac{1}{2} \int_{-k_F^2}^{k_F^2} \frac{dp}{2\pi} \int_{-k_F^2}^{k_F^2} \frac{dq}{2\pi} \Gamma_{-2Q+p+q} \left(\frac{q-p}{2}, \frac{q-p}{2} \right), \quad (\text{A25})$$

$$e_{\text{int}}^{+,-} = \frac{1}{2} \int_{-k_F^1}^{k_F^1} \frac{dp}{2\pi} \int_{-k_F^2}^{k_F^2} \frac{dq}{2\pi} \Gamma_{p+q} \left(-Q + \frac{q-p}{2}, -Q + \frac{q-p}{2} \right), \quad (\text{A26})$$

$$e_{\text{int}}^{-,+} = \frac{1}{2} \int_{-k_F^2}^{k_F^2} \frac{dp}{2\pi} \int_{-k_F^1}^{k_F^1} \frac{dq}{2\pi} \Gamma_{p+q} \left(Q + \frac{q-p}{2}, Q + \frac{q-p}{2} \right). \quad (\text{A27})$$

Because of the Pauli principle, the dominant contribution comes from the interaction between fermions with opposite momenta around $\pm Q$ in the low-density limit. The corresponding $O(\rho^3)$ contribution to the interaction energy density is:

$$e_{\text{int}}^{(1)} = 3e_0 \bar{\Lambda}_0 \Phi(\bar{\Lambda}_0, \bar{\delta}) (1 - \bar{\delta}^2), \quad (\text{A28})$$

where $\bar{\Lambda}_0 = \Lambda_0/k_F$ and

$$\Phi(\bar{\Lambda}_0, \bar{\delta}) = \iint_{-1}^1 \frac{dpdq}{4} \frac{1}{f\left(\frac{2\bar{\Lambda}_0}{p+q+\delta(p-q)}\right)}. \quad (\text{A29})$$

Therefore, the leading $O(\rho^3)$ contribution to the total energy density is

$$e_{\text{tot}}^{(1)} = e_{\text{kin}} + e_{\text{int}}^{(1)} = 3e_0 [\bar{\Lambda}_0 (\Phi(\bar{\Lambda}_0, \bar{\delta}) - \Phi(\bar{\Lambda}_0, 0)) + \bar{\delta}^2 (1 - \bar{\Lambda}_0 \Phi(\bar{\Lambda}_0, \bar{\delta}))] + \dots, \quad (\text{A30})$$

where we have omitted irrelevant constants. As we explained in the main text, the cut-off $\bar{\Lambda}_0$ must be chosen so that the $O(\rho^3)$ contribution to the energy density is independent of δ :

$$\bar{\Lambda}_0 (\Phi(\bar{\Lambda}_0, \bar{\delta}) - \Phi(\bar{\Lambda}_0, 0)) + \bar{\delta}^2 (1 - \bar{\Lambda}_0 \Phi(\bar{\Lambda}_0, \bar{\delta})) \equiv 0. \quad (\text{A31})$$

It can be shown numerically that this condition leads to a very weak dependence of $\bar{\Lambda}_0$ on the order parameter δ : $\bar{\Lambda}_0(\bar{\delta}) = a_0 + a_2 \bar{\delta}^2 + \dots$ with $a_0 \simeq 0.999991$, $a_2 \simeq -0.0552232$.

The $O(\rho^2)$ correction of the interacting vertex leads to an $O(\rho^4)$ contribution to the energy density:

$$e_{\text{int}}^{(2)} = g \rho^2 \rho_{-Q} \rho_{+Q} + u (\rho_{-Q}^3 \rho_{+Q} + \rho_{-Q} \rho_{+Q}^3) \quad (\text{A32})$$

$$+ w (\rho_{+Q}^4 + \rho_{-Q}^4), \quad (\text{A33})$$

where the first line arises from the interaction between fermions from different minima,

$$g = -\frac{\pi^4 \bar{\Lambda}_0^2 \Psi(\bar{\Lambda}_0, \bar{\delta}) D_2}{4m^{*2} D_1}, \quad (\text{A34})$$

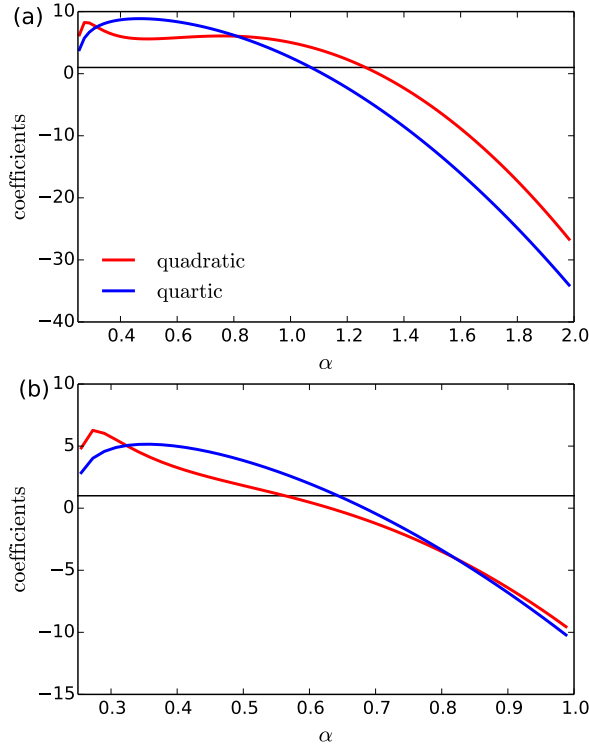


FIG. 12. (Color online) Coefficients of the quadratic (red) and quartic (blue) terms of the free-energy expansion Eq. (A39). The spin-exchange anisotropies are (a) $\Delta = 1$ and (b) $\Delta = 0.5$, corresponding to weak first-order and second-order transitions, respectively.

$$u = \frac{\pi^2 \sin^6(Q)}{6D_1^{(0)}(Q)}, \quad (\text{A35})$$

and the second line arises from the interaction between fermions from the same minimum

$$w = \frac{\pi^2 C}{12}. \quad (\text{A36})$$

The universal function $\Psi(\bar{\Lambda}_0, x)$ is given by

$$\Psi(\bar{\Lambda}_0, \bar{\delta}) = \frac{1}{4} \iint_{-1}^1 dp dq \frac{1}{f^2\left(\frac{2\bar{\Lambda}_0}{p+q+\bar{\delta}(p-q)}\right)}. \quad (\text{A37})$$

The dependence of g on $\bar{\delta}$ is as follows:

$$g(\bar{\Lambda}_0(\bar{\delta}), \bar{\delta}) = g_0 \left(1 + c_2 \bar{\delta}^2 + c_4 \bar{\delta}^4 + \dots\right), \quad (\text{A38})$$

where $g_0 = -\frac{1.10753 \times \pi^4 D_2}{4m^2 D_1}$, $c_2 \simeq -0.00290$ and $c_4 \simeq -0.00105$. In summary, given the renormalization condition (A31), the total free energy density is

$$f_{\text{tot}}(\delta) = f_{\text{tot}}(\delta = 0) + (3w - g_0(1 - c_2))\rho^2 \delta^2 + (2(w - u) - 4g_0(c_2 - c_4))\delta^4, \quad (\text{A39})$$

where

$$f_{\text{tot}}(\delta = 0) = \frac{2g_0 + u + w}{8}\rho^4 - \mu\rho \quad (\text{A40})$$

refers to the free energy of the normal state. The coefficients of the quadratic and quartic terms of the free energy expansion Eq. (A39) are shown in Fig. 12. Upon increasing α , the quartic coefficient becomes negative before the quadratic one for isotropic spin exchange ($\Delta = 1$). Correspondingly, the transition from the TLL2 phase to the vector chiral phase is of first order for $\Delta = 1$ and $\alpha_c \simeq 1.264$. The transition becomes continuous for $\Delta < \Delta_c \simeq 0.6684$, as indicated in Fig. 12(a).

¹ H. Diep, *Frustrated Spin Systems* (World Scientific, 2013).

² L. Balents, *Nature* **464**, 199 (2010).

³ L. Savary and L. Balents, **80**, 016502 (2017).

⁴ P. Chandra and P. Coleman, *Phys. Rev. Lett.* **66**, 100 (1991).

⁵ A. V. Chubukov, *Phys. Rev. B* **44**, 4693 (1991).

⁶ A. Läuchli, J. C. Domenge, C. Lhuillier, P. Sindzingre, and M. Troyer, *Phys. Rev. Lett.* **95**, 137206 (2005).

⁷ A. Läuchli, G. Schmid, and S. Trebst, *Phys. Rev. B* **74**, 144426 (2006).

⁸ T. Momoi, P. Sindzingre, and N. Shannon, *Phys. Rev. Lett.* **97**, 257204 (2006).

⁹ N. Shannon, T. Momoi, and P. Sindzingre, *Phys. Rev. Lett.* **96**, 027213 (2006).

¹⁰ T. Vekua, A. Honecker, H.-J. Mikeska, and F. Heidrich-Meisner, *Phys. Rev. B* **76**, 174420 (2007).

¹¹ L. Kecke, T. Momoi, and A. Furusaki, *Phys. Rev. B* **76**, 060407 (2007).

¹² D. Podolsky and E. Demler, *New Journal of Physics* **7**, 59 (2005).

¹³ M. E. Zhitomirsky and H. Tsunetsugu, *EPL (Europhysics Letters)* **92**, 37001 (2010).

¹⁴ A. Smerald and N. Shannon, *Phys. Rev. B* **88**, 184430 (2013).

¹⁵ O. A. Starykh and L. Balents, *Phys. Rev. B* **89**, 104407 (2014).

¹⁶ A. Kolezhuk and T. Vekua, *Phys. Rev. B* **72**, 094424 (2005).

¹⁷ I. P. McCulloch, R. Kube, M. Kurz, A. Kleine, U. Schollwöck, and A. K. Kolezhuk, *Phys. Rev. B* **77**, 094404 (2008).

¹⁸ J. Sudan, A. Läuchli, and A. M. Läuchli, *Phys. Rev. B* **80**, 140402 (2009).

¹⁹ T. Hikihara, T. Momoi, A. Furusaki, and H. Kawamura, *Phys. Rev. B* **81**, 224433 (2010).

²⁰ T. Hikihara, L. Kecke, T. Momoi, and A. Furusaki, *Phys. Rev. B* **78**, 144404 (2008).

²¹ S. Nishimoto, N. Shibata, and C. Hotta, *Nature Communications* **4**, 2287 (2013).

²² S. Furukawa, M. Sato, and S. Onoda, *Physical review letters* **105**, 257205 (2010).

²³ M. Sato, T. Momoi, and A. Furusaki, *Phys. Rev. B* **79**, 060406 (2009).

²⁴ A. Smerald and N. Shannon, *Phys. Rev. B* **93**, 184419 (2016).

²⁵ D. Hirobe, M. Sato, T. Kawamata, Y. Shiomi, K.-i. Uchida, R. Iguchi, Y. Koike, S. Maekawa, and E. Saitoh, *Nature Physics* **13**, 30 (2017).

²⁶ F. Heidrich-Meisner, I. P. McCulloch, and A. K. Kolezhuk, *Phys. Rev. B* **80**, 144417 (2009).

²⁷ A. K. Kolezhuk, F. Heidrich-Meisner, S. Greschner, and

- T. Vekua, Phys. Rev. B **85**, 064420 (2012).
- ²⁸ S. Furukawa, M. Sato, S. Onoda, and A. Furusaki, Physical Review B **86**, 094417 (2012).
 - ²⁹ F. Heidrich-Meisner, A. Honecker, and T. Vekua, Phys. Rev. B **74**, 020403 (2006).
 - ³⁰ R. Zinke, S.-L. Drechsler, and J. Richter, Phys. Rev. B **79**, 094425 (2009).
 - ³¹ J. Sirker, Phys. Rev. B **81**, 014419 (2010).
 - ³² M. Arlego, F. Heidrich-Meisner, A. Honecker, G. Rossini, and T. Vekua, Phys. Rev. B **84**, 224409 (2011).
 - ³³ S. Nishimoto, S.-L. Drechsler, R. O. Kuzian, J. van den Brink, J. Richter, W. E. A. Lorenz, Y. Skourski, R. Klingeler, and B. Büchner, Phys. Rev. Lett. **107**, 097201 (2011).
 - ³⁴ S. Nishimoto, S.-L. Drechsler, R. Kuzian, J. Richter, J. Málek, M. Schmitt, J. van den Brink, and H. Rosner, EPL (Europhysics Letters) **98**, 37007 (2012).
 - ³⁵ S. Nishimoto, S.-L. Drechsler, R. Kuzian, J. Richter, and J. van den Brink, Phys. Rev. B **92**, 214415 (2015).
 - ³⁶ F. Heidrich-Meisner, I. P. McCulloch, and A. K. Kolezhuk, Phys. Rev. B **80**, 144417 (2009).
 - ³⁷ M. Enderle, C. Mukherjee, B. Fåk, R. K. Kremer, J.-M. Broto, H. Rosner, S.-L. Drechsler, J. Richter, J. Malek, A. Prokofiev, W. Assmus, S. Pujol, J.-L. Raggazzoni, H. Rakoto, M. Rheinstädter, and H. M. Rønnow, EPL (Europhysics Letters) **70**, 237 (2005).
 - ³⁸ M. Enderle, B. Fåk, H.-J. Mikeska, R. K. Kremer, A. Prokofiev, and W. Assmus, Phys. Rev. Lett. **104**, 237207 (2010).
 - ³⁹ S.-L. Drechsler, S. Nishimoto, R. O. Kuzian, J. Málek, W. E. A. Lorenz, J. Richter, J. van den Brink, M. Schmitt, and H. Rosner, Phys. Rev. Lett. **106**, 219701 (2011).
 - ⁴⁰ M. Enderle, B. Fåk, H.-J. Mikeska, and R. Kremer, Phys. Rev. Lett. **106**, 219702 (2011).
 - ⁴¹ M. Mourigal, M. Enderle, B. Fåk, R. K. Kremer, J. M. Law, A. Schneidewind, A. Hiess, and A. Prokofiev, Phys. Rev. Lett. **109**, 027203 (2012).
 - ⁴² M. G. Banks, R. K. Kremer, C. Hoch, A. Simon, B. Ouladdiaf, J.-M. Broto, H. Rakoto, C. Lee, and M.-H. Whangbo, Phys. Rev. B **80**, 024404 (2009).
 - ⁴³ A. A. Gippius, E. N. Morozova, A. S. Moskvina, A. V. Zalessky, A. A. Bush, M. Baenitz, H. Rosner, and S.-L. Drechsler, Phys. Rev. B **70**, 020406 (2004).
 - ⁴⁴ S. Park, Y. J. Choi, C. L. Zhang, and S.-W. Cheong, Phys. Rev. Lett. **98**, 057601 (2007).
 - ⁴⁵ S.-L. Drechsler, O. Volkova, A. N. Vasiliev, N. Tristan, J. Richter, M. Schmitt, H. Rosner, J. Málek, R. Klingeler, A. A. Zvyagin, and B. Büchner, Phys. Rev. Lett. **98**, 077202 (2007).
 - ⁴⁶ S. E. Dutton, M. Kumar, M. Mourigal, Z. G. Soos, J.-J. Wen, C. L. Broholm, N. H. Andersen, Q. Huang, M. Zbiri, R. Toft-Petersen, and R. J. Cava, Phys. Rev. Lett. **108**, 187206 (2012).
 - ⁴⁷ H.-J. Grafe, S. Nishimoto, M. Iakovleva, E. Vavilova, L. Spillecke, A. Alfonsov, M.-I. Sturza, S. Wurmehl, H. Nojiri, H. Rosner, J. Richter, U. Rösler, S.-L. Drechsler, V. Kataev, and B. Büchner, Sci. Rep. **7**, 6720 (2017).
 - ⁴⁸ M. Schäpers, A. U. B. Wolter, S.-L. Drechsler, S. Nishimoto, K.-H. Müller, M. Abdel-Hafiez, W. Schottenhamel, B. Büchner, J. Richter, B. Ouladdiaf, M. Uhlarz, R. Beyer, Y. Skourski, J. Wosnitzer, K. C. Rule, H. Ryll, B. Klemke, K. Kiefer, M. Reehuis, B. Willenberg, and S. Süllo, Phys. Rev. B **88**, 184410 (2013).
 - ⁴⁹ B. Willenberg, M. Schäpers, A. U. B. Wolter, S.-L. Drechsler, M. Reehuis, J.-U. Hoffmann, B. Büchner, A. J. Studer, K. C. Rule, B. Ouladdiaf, S. Süllo, and S. Nishimoto, Phys. Rev. Lett. **116**, 047202 (2016).
 - ⁵⁰ E. Cemal, M. Enderle, R. K. Kremer, B. Fåk, E. Ressouche, J. P. Goff, M. V. Gvozdkova, M. E. Zhitomirsky, and T. Ziman, Phys. Rev. Lett. **120**, 067203 (2018).
 - ⁵¹ R. O. Kuzian, S. Nishimoto, S.-L. Drechsler, J. Málek, S. Johnston, J. van den Brink, M. Schmitt, H. Rosner, M. Matsuda, K. Oka, H. Yamaguchi, and T. Ito, Phys. Rev. Lett. **109**, 117207 (2012).
 - ⁵² N. Motoyama, H. Eisaki, and S. Uchida, Phys. Rev. Lett. **76**, 3212 (1996).
 - ⁵³ M. Matsuda, K. Katsumata, K. M. Kojima, M. Larkin, G. M. Luke, J. Merrin, B. Nachumi, Y. J. Uemura, H. Eisaki, N. Motoyama, S. Uchida, and G. Shirane, Phys. Rev. B **55**, R11953 (1997).
 - ⁵⁴ I. A. Zaliznyak, H. Woo, T. G. Perring, C. L. Broholm, C. D. Frost, and H. Takagi, Phys. Rev. Lett. **93**, 087202 (2004).
 - ⁵⁵ G. Castilla, S. Chakravarty, and V. J. Emery, Phys. Rev. Lett. **75**, 1823 (1995).
 - ⁵⁶ J. V. Alvarez and C. Gros, Phys. Rev. Lett. **89**, 156603 (2002).
 - ⁵⁷ F. Heidrich-Meisner, A. Honecker, D. C. Cabra, and W. Brenig, Phys. Rev. B **66**, 140406 (2002).
 - ⁵⁸ F. Heidrich-Meisner, A. Honecker, D. C. Cabra, and W. Brenig, Phys. Rev. B **68**, 134436 (2003).
 - ⁵⁹ E. Orignac, R. Chitra, and R. Citro, Phys. Rev. B **67**, 134426 (2003).
 - ⁶⁰ K. Saito, Phys. Rev. B **67**, 064410 (2003).
 - ⁶¹ E. Shimshoni, N. Andrei, and A. Rosch, Phys. Rev. B **68**, 104401 (2003).
 - ⁶² X. Zotos, Phys. Rev. Lett. **92**, 067202 (2004).
 - ⁶³ A. V. Rozhkov and A. L. Chernyshev, Phys. Rev. Lett. **94**, 087201 (2005).
 - ⁶⁴ A. Klümper and K. Sakai, J. Phys. A: Math. Gen. **35**, 2173 (2002).
 - ⁶⁵ K. Sakai and A. Klümper, J. Phys. A: Math. Gen. **36**, 11617 (2003).
 - ⁶⁶ K. Louis and C. Gros, Phys. Rev. B **67**, 224410 (2003).
 - ⁶⁷ K. Sakai and A. Klümper, J. Phys. Soc. Jpn. Suppl. **74**, 196 (2005).
 - ⁶⁸ Y. Kohama, A. V. Sologubenko, N. R. Dilley, V. S. Zapf, M. Jaime, J. A. Mydosh, A. Paduan-Filho, K. A. Al-Hassanieh, P. Sengupta, S. Gangadharaiyah, A. L. Chernyshev, and C. D. Batista, Phys. Rev. Lett. **106**, 037203 (2011).
 - ⁶⁹ A. V. Sologubenko, K. Giannò, H. R. Ott, U. Ammerahl, and A. Revcolevschi, Phys. Rev. Lett. **84**, 2714 (2000).
 - ⁷⁰ C. Hess, C. Baumann, U. Ammerahl, B. Büchner, F. Heidrich-Meisner, W. Brenig, and A. Revcolevschi, Phys. Rev. B **64**, 184305 (2001).
 - ⁷¹ K. Kudo, S. Ishikawa, T. Noji, T. Adachi, Y. Koike, K. Maki, S. Tsuji, and K. ichi Kumagai, Journal of the Physical Society of Japan **70**, 437 (2001).
 - ⁷² A. V. Sologubenko, E. Felder, K. Giannò, H. R. Ott, A. Vietkine, and A. Revcolevschi, Phys. Rev. B **62**, R6108 (2000).
 - ⁷³ A. V. Sologubenko, K. Giannò, H. R. Ott, A. Vietkine, and A. Revcolevschi, Phys. Rev. B **64**, 054412 (2001).
 - ⁷⁴ A. V. Sologubenko, H. R. Ott, G. Dhalenne, and A. Revcolevschi, EPL (Europhysics Letters) **62**, 540 (2003).
 - ⁷⁵ C. Hess, H. ElHaes, A. Waske, B. Büchner, C. Sekar, G. Krabbes, F. Heidrich-Meisner, and W. Brenig, Phys. Rev. Lett. **98**, 027201 (2007).
 - ⁷⁶ C. Hess, H. ElHaes, B. Büchner, U. Ammerahl, M. Hücker, and A. Revcolevschi, Phys. Rev. Lett. **93**, 027005 (2004).
 - ⁷⁷ N. Hlubek, P. Ribeiro, R. Saint-Martin, A. Revcolevschi, G. Roth, G. Behr, B. Büchner, and C. Hess, Phys. Rev. B **81**, 020405 (2010).
 - ⁷⁸ C. Hess, Eur. Phys. J. Spec. Topics **151**, 73 (2008).
 - ⁷⁹ A. V. Sologubenko, T. Lorenz, H. R. Ott, and A. Freimuth, J.

- Low Temp. Phys. **147**, 387 (2007).
- ⁸⁰ X. Zotos, F. Naef, and P. Prelovšek, Phys. Rev. B **55**, 11029 (1997).
 - ⁸¹ F. Heidrich-Meisner, A. Honecker, D. C. Cabra, and W. Brenig, Phys. Rev. Lett. **92**, 069703 (2004).
 - ⁸² R. Steinigeweg, J. Herbrych, and P. Prelovšek, Phys. Rev. E **87**, 012118 (2013).
 - ⁸³ R. Steinigeweg, J. Herbrych, X. Zotos, and W. Brenig, Phys. Rev. Lett. **116**, 017202 (2016).
 - ⁸⁴ P. Jung, R. W. Helmes, and A. Rosch, Phys. Rev. Lett. **96**, 067202 (2006).
 - ⁸⁵ A. A. Aligia, C. D. Batista, and F. H. L. Eßler, Phys. Rev. B **62**, 3259 (2000).
 - ⁸⁶ F. Heidrich-Meisner, A. Honecker, and W. Brenig, Phys. Rev. B **71**, 184415 (2005).
 - ⁸⁷ S. Langer, R. Darradi, F. Heidrich-Meisner, and W. Brenig, Phys. Rev. B **82**, 104424 (2010).
 - ⁸⁸ C. Psaroudaki and X. Zotos, Journal of Statistical Mechanics: Theory and Experiment **2016**, 063103 (2016).
 - ⁸⁹ A. V. Sologubenko, T. Lorenz, J. A. Mydosh, B. Thielemann, H. M. Rønnow, C. Rüegg, and K. W. Krämer, Phys. Rev. B **80**, 220411 (2009).
 - ⁹⁰ K. Okunishi and T. Tonegawa, J. Phys. Soc. Jpn. **72**, 479 (2003).
 - ⁹¹ K. Okunishi, J. Phys. Soc. Jpn. **77**, 114004 (2008).
 - ⁹² K. Okamoto and K. Nomura, Physics Letters A **169**, 433 (1992).
 - ⁹³ S. R. White and I. Affleck, Phys. Rev. B **54**, 9862 (1996).
 - ⁹⁴ S. Eggert, Phys. Rev. B **54**, R9612 (1996).
 - ⁹⁵ P. Jordan and E. Wigner, Zeitschrift für Physik **47**, 631 (1928).
 - ⁹⁶ J. Takeya, I. Tsukada, Y. Ando, T. Masuda, K. Uchinokura, I. Tanaka, R. S. Feigelson, and A. Kapitulnik, Phys. Rev. B **63**, 214407 (2001).
 - ⁹⁷ M. Hofmann, T. Lorenz, A. Freimuth, G. S. Uhrig, H. Kageyama, Y. Ueda, G. Dhalenne, and A. Revcolevschi, Physica B **312-313**, 597 (2002).
 - ⁹⁸ M. Pustilnik, E. G. Mishchenko, L. I. Glazman, and A. V. Andreev, Phys. Rev. Lett. **91**, 126805 (2003).
 - ⁹⁹ M. Pustilnik, M. Khodas, A. Kamenev, and L. I. Glazman, Phys. Rev. Lett. **96**, 196405 (2006).
 - ¹⁰⁰ J. Lin, K. A. Matveev, and M. Pustilnik, Phys. Rev. Lett. **110**, 016401 (2013).
 - ¹⁰¹ A. V. Sologubenko, K. Berggold, T. Lorenz, A. Rosch, E. Shimshoni, M. D. Phillips, and M. M. Turnbull, Phys. Rev. Lett. **98**, 107201 (2007).
 - ¹⁰² E. Boulat, P. Mehta, N. Andrei, E. Shimshoni, and A. Rosch, Phys. Rev. B **76**, 214411 (2007).
 - ¹⁰³ A. L. Chernyshev and A. V. Rozhkov, Phys. Rev. B **72**, 104423 (2005).
 - ¹⁰⁴ A. L. Chernyshev and W. Brenig, Phys. Rev. B **92**, 054409 (2015).
 - ¹⁰⁵ A. L. Chernyshev and A. V. Rozhkov, Phys. Rev. Lett. **116**, 017204 (2016).
 - ¹⁰⁶ G. D. Mahan, *Many particle physics*, 3 (Plenum Press, New York London, 1980).
 - ¹⁰⁷ B. S. Shastry, Phys. Rev. B **73**, 085117 (2006).
 - ¹⁰⁸ C. Psaroudaki, J. Herbrych, J. Karadamoglou, P. Prelovšek, X. Zotos, and N. Papanicolaou, Phys. Rev. B **89**, 224418 (2014).
 - ¹⁰⁹ S. Sachdev, *Quantum Phase Transitions* (Cambridge University Press, 2011).
 - ¹¹⁰ K. Maisinger and U. Schollwöck, Phys. Rev. Lett. **81**, 445 (1998).
 - ¹¹¹ N. Maeshima and K. Okunishi, Phys. Rev. B **62**, 934 (2000).
 - ¹¹² A. E. Feiguin and S. R. White, Phys. Rev. B **72**, 220401 (2005).